LSD1 represses a neonatal/reparative gene program in adult intestinal epithelium

Rosalie T. Zwiggelaar[1,13], Håvard T. Lindholm[1,13], Madeleine Fosslie[2,14], Marianne T. Pedersen[3,14], Yuki Ohta[4,5,14], Alberto Díez-Sánchez[1], Mara Martín-Alonso[1], Jenny Ostrop[1], Mami Matano[4,5], Naveen Parmar[1], Emilie Kvaløy[1], Roos R. Spanjers[1], Kamran Nazmi[6], Morten Rye[7,8], Finn Drabløs[7], Cheryl Arrowsmith[9,10,11], John Arne Dahl[2], Kim B. Jensen[3,12], Toshiro Sato[3,4], Menno J. Oudhoff[1*]

[1]CEMIR – Centre of Molecular Inflammation Research, Department of Clinical and Molecular Medicine, NTNU – Norwegian University of Science and Technology, 7491 Trondheim, Norway

[2]Department of Microbiology, Oslo University Hospital, Rikshospitalet, NO-0027, Oslo, Norway.

[3]BRIC: Biotech Research and Innovation Centre, University of Copenhagen, DK-2200 Copenhagen N, Denmark

[4]Department of Gastroenterology, Keio University School of Medicine, Tokyo 160-8582, Japan

[5]Department of Organoid Medicine, Keio University School of Medicine, Tokyo 160-8582, Japan

[6]Department of Oral Biochemistry, Academic Centre for Dentistry (ACTA), 1081LA Amsterdam, The Netherlands.

[7]Department of Clinical and Molecular Medicine, NTNU – Norwegian University of Science and Technology, 7491 Trondheim, Norway

[8]Clinic of Surgery, St. Olav's Hospital, Trondheim University Hospital, 7030 Trondheim, Norway

[9]Structural Genomics Consortium, University of Toronto, Toronto, ON, M5G 1L7, Canada.

[10]Princess Margaret Cancer Centre, University Health Network, Toronto, ON, M5G 2M9, Canada.

[11]Department of Medical Biophysics, University of Toronto, Toronto, ON, M5G 1L7, Canada.

[12]Novo Nordisk Foundation Center for Stem Cell Research, Faculty of Medical and Health, University of Copenhagen, DK-2200 Copenhagen N, Denmark

[13]These authors contributed equally

[14]These authors contributed equally

[*] corresponding author, e-mail: menno.oudhoff@ntnu.no

SUMMARY

Intestinal epithelial homeostasis is maintained by adult intestinal stem cells, which, alongside Paneth cells, appear after birth. It is unclear how neonatal intestinal epithelial development is regulated. We found that Lysine-specific demethylase 1A (*Kdm1a/Lsd1*) is required for the postnatal maturation of crypts, including Paneth cell differentiation. *Lsd1*-deficient epithelium retains a neonatal state into adulthood, which is beneficial for repair after irradiation injury. *Lsd1*-deficient crypts, devoid of Paneth cells, are still able to form and maintain organoids. Mechanistically, we find a spatiotemporal expression of LSD1 during crypt formation, and LSD1 represses genes that are normally expressed in fetal and neonatal epithelium. Surprisingly, we could not link the transcriptional control by LSD1 functionally to fetal- or neonatal specific H3K4me1 sites. Nevertheless, enzymatic inhibition of LSD1 also leads to a loss of Paneth cells and increase in LGR5-expressing cells in human organoids. In summary, we found an important regulator of neonatal intestinal development and identified a druggable target to reprogram intestinal epithelium towards a reparative state.

45 **INTRODUCTION**

46 The intestinal epithelium undergoes a dramatic change during the neonatal period. Crypt
47 formation occurs after birth together with the appearance of Paneth cells (PCs) and the
48 development of adult intestinal stem cells (ISCs). Adult ISCs rely on niche factors such as
49 Wnt ligands. *In vivo,* mesenchymal cells are important sources of Wnt to support ISC
50 maintenance (Degirmenci et al., 2018; Greicius et al., 2018; Shoshkes-Carmel et al., 2018),
51 whereas *in vitro*, it is PCs that are required to supply the necessary Wnt (Durand et al., 2012;
52 Farin et al., 2012; Kim et al., 2012; Sato et al., 2011). In contrast, Wnt ligands or PCs are
53 dispensable for fetal organoid homeostasis (Fordham et al., 2013; Mustata et al., 2013). Thus,
54 ISCs undergo a fetal-to-adult transition that includes a change in Wnt dependency.
55
56 Recently, the existence of bona fide fetal ISCs has been challenged by the finding that any
57 fetal epithelial cell can be or become an adult ISC as long as the appropriate environment is
58 supplied (Guiu et al., 2019). This model fits nicely with studies showing that after injury, the
59 intestinal epithelium is temporarily reprogrammed into a fetal-like state that is needed for
60 proper repair (Gregorieff et al., 2015; Nusse et al., 2018; Yui et al., 2018). This, in turn,
61 complements work specifying that adult intestinal epithelial lineages can dedifferentiate to
62 give rise to new ISCs to rebuild the epithelium after injury (Buczacki et al., 2013; Tetteh et
63 al., 2016; van Es et al., 2012; S. Yu et al., 2018). In hindsight, these high levels of cell-fate
64 reversion make sense because the intestine is a common site for chemical and mechanical
65 challenges as well as the host for many putative pathogens. Nonetheless, it is not yet fully
66 understood how the fetal-to-adult ISC transition, or its reversal upon injury, is mediated, and
67 whether epithelial reprogramming can be targeted therapeutically.
68
69 Adult ISCs give rise to all intestinal epithelial subtypes. Unlike other stem cell systems, both
70 ISCs and differentiating intestinal epithelial cells have a similar chromatin state at lineage
71 defining genes, which allows for Notch-mediated lateral inhibition in ISC differentiation
72 (Kim et al., 2014). However, the same group subsequently identified differences in open
73 chromatin distinguishing ISCs from secretory precursors, which was reversed upon
74 irradiation when these secretory precursors dedifferentiate into ISCs (Jadhav et al., 2017).
75 Three groups separately identified a crucial role for the polycomb repressive complex 2
76 (PRC2) in maintaining crypt physiology (Chiacchiera et al., 2016; Jadhav et al., 2019;
77 Koppens et al., 2016). Although some epigenetic modifiers, such as the PRC2 complex, are
78 critical, others, such as DOT1L, play a minimal role in maintaining intestinal epithelial

physiology (Ho et al., 2013). In summary, although it is clear there is an important role for certain epigenetic modifiers in intestinal epithelial biology, the role and importance of others remain undefined.

Here we exploit the availability of chemical probes targeting epigenetic modifiers (Scheer et al., 2018), and combine it with intestinal organoid cultures (Sato et al., 2009), to identify the demethylase LSD1 as a critical regulator of crypt maturation including PC differentiation. LSD1 is a demethylase of H3K4me1/2 that is known to 'decommission' enhancers during embryonic development (Agarwal et al., 2017; Whyte et al., 2012). We observe that LSD1 itself is tightly regulated and its levels are reduced during crypt formation, both in development and after injury, yet, our data suggests that LSD1 is not required for the decommissioning of H3K4me1 sites that occurs during intestinal epithelial development. Nevertheless, mice lacking *Lsd1* in the intestinal epithelium have crypts resembling newly formed crypts that lack PCs and are filled with ISC-like cells.

RESULTS

Identification of LSD1 as a regulator of Paneth cell differentiation

The intestinal epithelium undergoes a dramatic change during the neonatal period including the appearance of Paneth cells (PCs) two weeks after birth. To study PC differentiation in organoids, we developed a differentiation protocol (adapted from (Yin et al., 2013)) using CHIR (GSK3 inhibitor) and DAPT (γ-secretase inhibitor) to activate Wnt and block Notch signalling, respectively (Fig. S1A). CHIR-DAPT treatment led to a robust enrichment of Lysozyme^{+} PCs by confocal microscopy, mRNA, and protein expression compared to standard EGF, Noggin, and R-spondin 1 (ENR) organoid growing conditions (Fig. 1A, S1B, S1C). Next, we tested chemical probes targeting 18 methyltransferases and demethylases and identified the LSD1 inhibitor GSK-LSD1 to consistently repress PC differentiation (Fig. 1B, 1C, S1D-G, Supplementary table 1). In support, GSK-LSD1 similarly affected PC differentiation in organoids grown in ENR conditions (Fig. 1D, S1H). Use of a different LSD1 inhibitor led to a similar near loss of PCs (Fig. S1I). Consistent with the irreversible binding nature of GSK-LSD1 to its target (Mohammad et al., 2015), we found that upon withdrawal of GSK-LSD1, PCs re-appeared after 2 organoid splitting events (Fig. 1E, S1J). To test if only a selection or all PC genes are downregulated upon LSD1 inhibition, we performed RNA-seq on organoids treated with GSK-LSD1 for 24 h, between day 1 and 2

112 after splitting, which we anticipate is right when PCs develop in organoids. We found a
113 robust downregulation of all PC specific genes (gene set from (Haber et al., 2017)) (Fig. 1F).
114 In contrast, we did not observe change in expression of genes recently identified to be
115 important for breaking of symmetry (Serra et al., 2019)(Fig. 1G). This could explain why we
116 still observe budding and crypt formation, even in the absence of new PC formation.
117
118 **Inhibition of LSD1 renders Lgr5$^+$ cells independent of niche-providing PCs *in vitro*.**
119 PCs are crucial for adult small intestinal organoid growth as they supply niche factors to
120 retain a stem cell population, and normally, PC-devoid organoids only sustain growth upon
121 Wnt supplementation (Durand et al., 2012; Farin et al., 2012; Kim et al., 2012; Sato et al.,
122 2011). To test the role of LSD1 in intestinal stem cells, we used Lgr5-EGFP derived
123 organoids and treated them with GSK-LSD1. We found that GSK-LSD1 treatment resulted in
124 a 2-3 fold increase in percentage of Lgr5$^+$ cells (Fig. 1H, 1I, S1K), and co-treatment of GSK-
125 LSD1 with CHIR or valproic acid had an additive effect on the Lgr5$^+$ population (Fig. S1K).
126 Thus, GSK-LSD1 treatment expands the Lgr5$^+$ population and renders these cells
127 independent of PC-derived niche factors such as *Wnt3* (Fig. S1L). To test if GSK-LSD1 is
128 able to act like Wnt ligands we quantified clonal organoid formation from single sorted Lgr5$^+$
129 cells. However, unlike Wnt3A, GSK-LSD1 is not able to increase organoid formation from
130 single cells (Fig. 1J). In addition, in contrast to the rapid loss of PC differentiation, 24 h
131 GSK-LSD1 treatment did not lead to an expansion of the Lgr5$^+$ population (Fig. 1K). Thus,
132 this feature does not precede PC loss. Nevertheless, using a recently described culture
133 condition that allows PC differentiation in human organoids (Fujii et al., 2018), we found that
134 GSK-LSD1 also blocks PC differentiation in human organoids while simultaneously
135 expanding the LGR5$^+$ population (Fig. 1L, 1M). Together, we identify that inhibition of
136 LSD1 leads to a loss of PCs and an increase of Lgr5$^+$ cells in organoids, and our data
137 suggests this occurs separately from Wnt or Notch pathway activation.

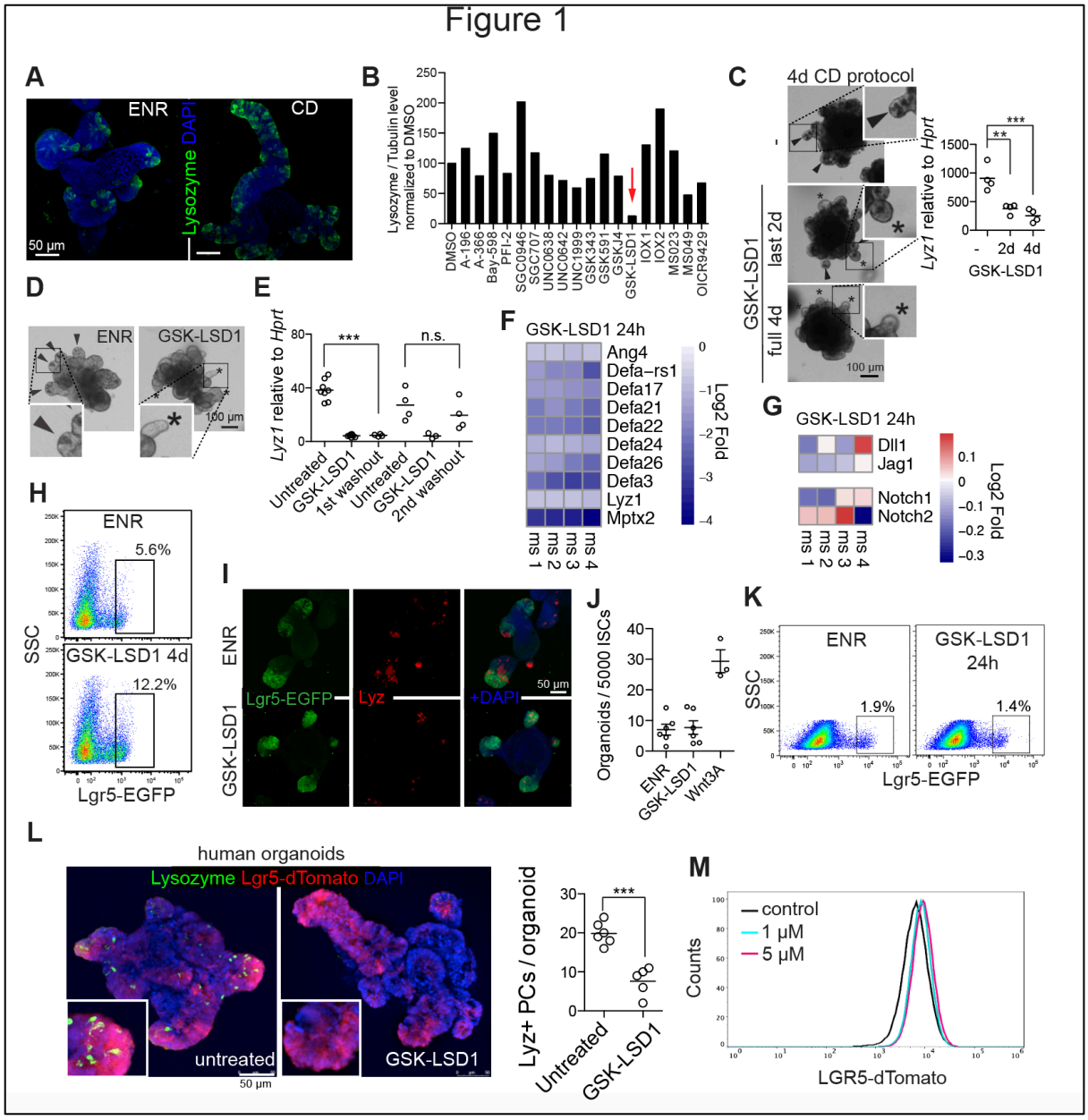

Fig. 1 | Inhibition of LSD1 blocks PC differentiation and allows niche-independent expansion of ISCs. A, Confocal images of Lysozyme and DAPI staining of ENR and CHIR-DAPT (CD protocol as in (S1A)) grown organoids. **B,** Quantification of Lysozyme/Tubulin levels by western blot of organoids treated with indicated inhibitors in CD conditions. Concentrations used can be found in supplementary table 1. Data is mean from 2 independent experiments (see Fig. S1D for raw data). **C,** Brightfield images and inserts of CD-grown organoids, supplemented with GSK-LSD1 (1 µM) for the last 2 days (2d) or throughout experiment (4d). *Lyz1* expression relative to *Hprt* by qPCR. **C&D**, Arrows indicate PC^{+} crypts based on presence of granular cells, asterisks indicate PC^{-} crypts. **D,** Brightfield images and inserts of ENR-grown organoids with or without GSK-LSD1 (1 µM). **E,** *Lyz1* expression relative to *Hprt* by qPCR. **F & G** Heatmaps of indicated genes from RNA-seq of 24 h GSK-LSD1 treated organoids. N=4 different mouse organoid lines, and expression is relative to each individual control. **H&K,** Flow cytometry of Lgr5-EGFP organoids. Representative plot from at least n=3 different mouse lines. **I,** Images of Lgr5-EGFP (anti-GFP) and Lyz (Lysozyme) staining of organoids. **J,** Organoid outgrowth from single sorted Lgr5^{HIGH} ISCs, each dot represents a mouse, data pooled from 3 independent experiments.

152 Mean and SE are shown. **L,** Images of human LGR5-dTomato organoids, additionally stained for Lysozyme.
153 Quantified number of PCs per human organoid from 2 different experiments. **M,** Flow cytometry of LGR5-
154 dTomato treated human organoids with 1 or 5 μM. ** $p<0.01$ ***$p<0.001$
155

156 **Spatiotemporal expression of LSD1 during postnatal development**

157 In adult mouse epithelium, we observed a clear enrichment of LSD1 expression in crypts
158 compared to villi (Fig. S2A, S2B). However, we did observe LSD1-negative cells at the
159 bottom of crypts, which is where ISCs and PCs reside. Therefore, we examined the
160 expression of LSD1 using intestinal tissue and organoids derived from *Lgr5*-EGFP mice to
161 mark ISCs (Barker et al., 2007). We found that LSD1 is markedly absent from PCs both *in*
162 *vivo* and *in vitro*, whereas LSD1 was detected in nuclei of all other crypt cells including
163 Lgr5$^+$ ISCs (Fig. 2A, 2B). A major part of intestinal epithelial development occurs after birth,
164 including crypt formation, PC differentiation, and appearance of adult Lgr5$^+$ ISCs. We
165 observed a change in the LSD1 expression pattern when we compared P7 and P21
166 developmental stages (Fig. 2C). Specifically, at P7 we see robust expression of LSD1 in
167 villus regions with reduced LSD1 expression in the zone where newly forming crypts appear
168 (Fig. 2C). In contrast, at P21 the LSD1 pattern resembles adulthood with an enrichment in the
169 crypt region compared to the villi (Fig. 2C, S2A).
170

171 **LSD1 is required for PCs but not goblet or enteroendocrine cells *in vivo***

172 To test the role of LSD1 *in vivo,* we crossed *Lsd1*$^{f/f}$ (Kerenyi et al., 2013) with *Villin*-Cre
173 mice to delete *Lsd1* in intestinal epithelial cells specifically (KO mice). Although these mice
174 appear normal, we found that KO mice lack PCs throughout the small intestine (Fig. 2D,
175 S2C). We did observe that KO mice had 'escaper' crypts still expressing LSD1, and LSD1$^+$
176 crypts were positive for Lysozyme (Fig. S2D). Thus, these mice do not completely lack PCs.
177 Currently, two genes are known to be absolutely required for PC differentiation *in vivo; Sox9*
178 and *Atoh1* (Bastide et al., 2007; Yang et al., 2001). We did not observe differences in Sox9
179 expression (Fig. 2D), and, although we found fewer *Atoh1*$^+$ cells in KO epithelium (Fig. 2D),
180 reduction of *Atoh1*$^+$ cells unlikely causes a complete lack of PCs. We reasoned that perhaps
181 KO crypts are filled with PC precursors expressing *Wnt3*, however, similar to GSK-LSD1
182 treated organoids, *Wnt3* was markedly reduced in crypts of KO mice except for Lsd1$^+$
183 escaper crypts (Fig. 2D, S2E).
184

185 Next, we examined other intestinal secretory lineages and found a reduction of goblet cells,
186 but equal numbers of enteroendocrine cells, comparing adult WT and KO littermates (Fig.
187 2E). When we examined fetal and postnatal intestines of WT and KO littermates, we found
188 that the reduction in goblet cells emerges after developmental stage P7, similar to when PCs
189 develop (Fig. 2F, S2F, S2G). These results suggest that LSD1 KO epithelium maintains
190 neonatal characteristics into adulthood, including the absence of PCs and fewer goblet cells.
191

192 **Mice lacking LSD1 sustain crypt-bottom ISCs independent of PCs, and KO organoids**
193 **grow independent of endogenous Wnt**

194 To test the role of LSD1 in ISCs *in vivo,* we used *in situ* hybridization (ISH) and antibody-
195 based detection of the ISC marker *Olfm4* in tissues of WT and KO mice. We found Olfm4^{+}
196 cells completely filling the bottom of crypts in KO mice, compared to the standard PC/ISC
197 pattern observed in WT crypts (Fig. 2G, S2H). In addition, all crypt-base cells in KO mice
198 are Ki67^{+}, suggesting that these Olfm4^{+} cells are proliferating (Fig. S2H). *Atoh1*$^{-/-}$ mice lack
199 PCs, and *Atoh1*$^{-/-}$ crypts do not sustain organoid growth without Wnt supplementation
200 (Durand et al., 2012). In contrast, *Lsd1* WT and KO crypts were equally able to form
201 organoids, even in the absence of PCs in KO organoids (Fig. 2H). This led us to hypothesize
202 that KO organoids do not rely on endogenous Wnt. Indeed, blockage of Wnt signaling by the
203 porcupine inhibitor IWP-2, showed that treated KO organoids sustained growth unlike WT
204 organoids (Fig. 2I, 2J). Of note, IWP-2 distinctively reduced growth rate in KO organoids,
205 which makes long-term expansion unfeasible, yet, after splitting there were still surviving KO
206 organoids under continuous IWP-2 treatment, and, LSD1 inhibitor treatment greatly
207 increased splitting efficiency (Fig. S2I, S2J). In contrast, both KO and WT organoids could
208 not sustain growth in medium lacking R-spondin 1 (Fig. 2I, 2J).

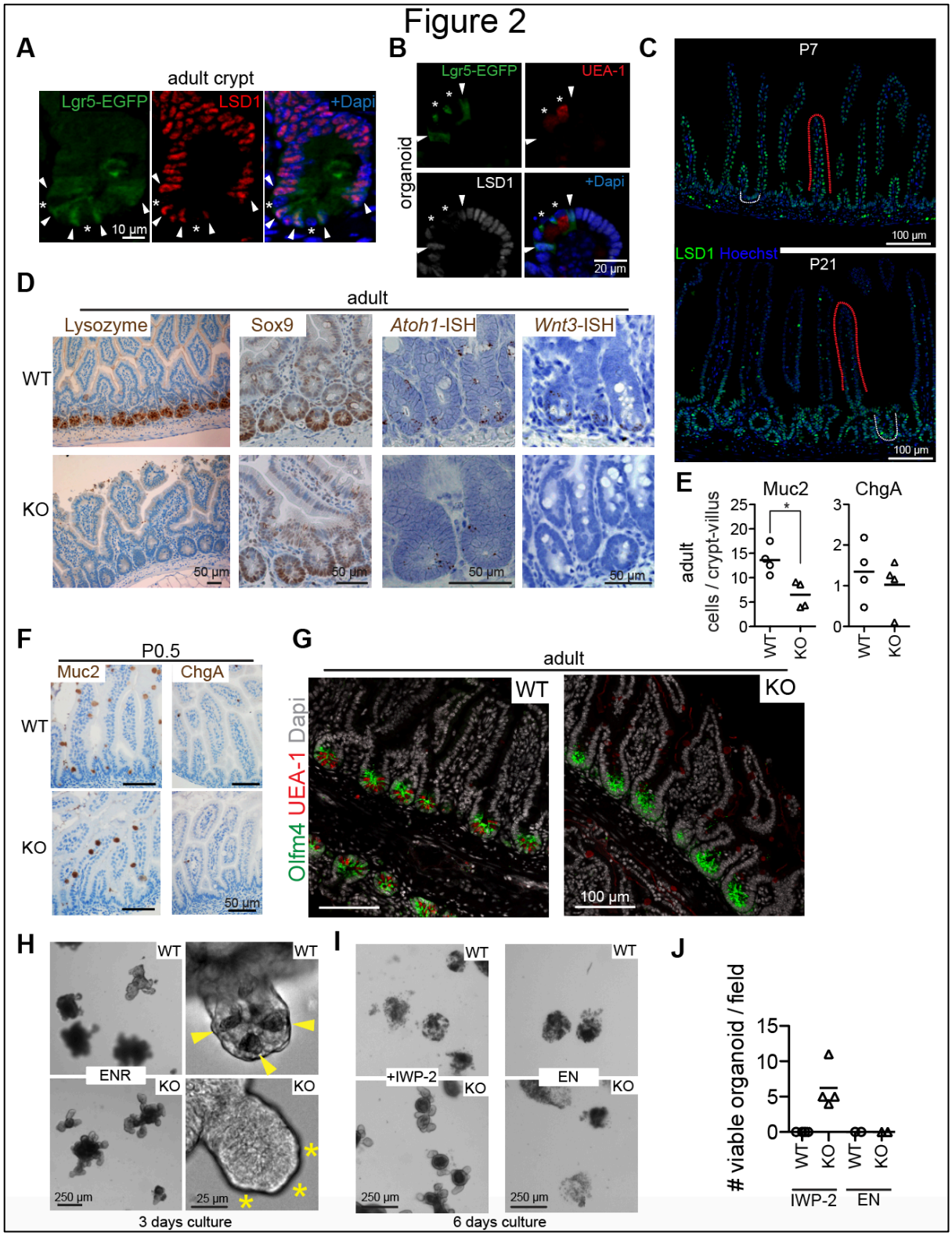

Fig. 2 | LSD1 localization and expression is linked to crypt maturation *in vivo* and Wnt dependency of organoids. A&B Images of Lgr5-EGFP (anti-GFP), Lsd1, and Ulex Europea Agglutinin 1 (UEA-1, to detect PCs) staining of adult duodenum crypts (A) and organoids (B). **C,** Images of Lsd1 staining of tissue harvested at P7 and P21. White dotted lines indicate crypts, red dotted lines indicate villi. **D,** Representative images of antibody (Lysozyme and Sox9) and *in situ* hybridization (ISH) (*Atoh1* and *Wnt3*) staining of WT and KO duodenum tissue. **E,** Quantification of Muc2^{+} goblet and ChgA^{+} enteroendocrine cells in adult duodenum

216 intestine. N=4 mice, *p<0.05. **F,** Representative images of Muc2 and ChgA antibody staining at P0.5 (for
217 quantification see Fig. S2F). **G,** Representative image of Olfm4 antibody and UEA-1 staining of adult WT and
218 KO tissue. **H-J,** Brightfield images of WT and KO organoids with indicated treatments, quantified are wells
219 from 2 different experiments (n=2 mice).
220

221 **LSD1 represses a fetal-like, reparative gene program that allows PC differentiation**
222 **independent of YAP/TAZ**

223 Next, we sought to find the mechanism by which LSD1 controls intestinal epithelial biology.
224 We performed RNA-seq on FACS-sorted Epcam^{+} small intestinal crypt cells from WT and
225 KO mice. We found 2564 up and 1522 down regulated genes (p-adj<0.1) in KO cells
226 compared to WT cells (Fig. 3A). In support of our findings that there are *Atoh1*$^{+}$ cells in KO
227 crypts and the differential ability of *Atoh1*-KO and *Lsd1*-KO crypts to form organoids, we
228 found no shift towards an *Atoh1*$^{-/-}$ gene signature in the KO transcriptional profile (Fig. S3A)
229 (Kim et al., 2014). To verify our gene expression profile, we tested a PC-specific gene
230 signature (Haber et al., 2017), and, expectedly, found that this is suppressed in KO crypts
231 (Fig. 3B). However, an Lgr5-ISC signature gene set (Muñoz et al., 2012) was not enriched in
232 our KO transcript profile (Fig. 3C). Over the years, there have been various different
233 intestinal stem cell and stem-cell like populations described, either using genetic markers
234 such as Bmi1, or by techniques such as label-retaining capacity and scRNA-seq (Ayyaz et al.,
235 2019; Buczacki et al., 2013; van Es et al., 2012; Yan et al., 2017). To test if there was
236 enrichment for a certain stem cell type, we analyzed expression of defining genes for each
237 population (Fig. S3B), however, we did not find enrichment for any stem cell subtype.
238

239 Recently, two groups elegantly identified and characterized a cellular repair state in the
240 intestinal epithelium (Nusse et al., 2018; Yui et al., 2018). Indeed, two repair gene signatures
241 from these studies were enriched in the KO transcriptional profile (Fig. 3D). These reparative
242 profiles are fetal-like, and, in support, we also find enrichment of two fetal gene sets in the
243 KO transcriptional profile (Fig. 3E) (Mustata et al., 2013; Yui et al., 2018), with clear
244 enrichment of defining markers specifically identified in these studies (Fig. 3F). Yui *et al.*
245 revealed that the reparative state was mediated by YAP/TAZ (Yui et al., 2018). Indeed, a
246 separate YAP gene signature was enriched in our KO transcriptional profile (Fig. 3G)
247 (Gregorieff et al., 2015). To test if YAP/TAZ is required for LSD1-mediated PC
248 differentiation, we treated organoids derived from mice lacking both *Yap* and the gene
249 encoding for TAZ *Wwtr1* (*Vil*-Cre;*Yap*$^{f/f}$;*Wwtr1*$^{f/f}$) with GSK-LSD1 and found that PC

250 differentiation was equally impaired in WT and mutant organoids (Fig. S3C). However, we
251 noted that approximately half of these organoids contained *Yap* and *Wwtr1* based on qPCR
252 (Fig. S3D). We thus tested a second model, deleting YAP/TAZ in an inducible manner (*Vil*-
253 CreERT2; *Yap*$^{f/f}$;*Wwtr1*$^{f/f}$ organoids). Indeed, tamoxifen treatment led to near undetectable
254 levels of both *Yap* and *Wwtr1* (Fig. S3E), impaired survival and led to an increase in PCs
255 (Fig. 3H, 3I), in accordance with previous results (Azzolin et al., 2014; Gregorieff et al.,
256 2015). Strikingly, GSK-LSD1 treatment completely abrogated PC differentiation
257 independently of YAP/TAZ (Fig. 3H, 3I).
258
259 **LSD1 represses GFI1 mediated genes**
260 We observed a rapid and broad reduction of Paneth cell genes upon GSK-LSD1 treatment
261 (Fig. 1F), however, we did not observe an increase of Lgr5^{+} cells within that same timeline
262 (Fig. 1K). In support, we also do not observe enrichment of both fetal gene programs after
263 24h of GSK-LSD1 treatment (Fig. 3J), suggesting this requires sustained inhibition or
264 deletion of LSD1. Nevertheless, a study recently reported that an LSD1-GFI1 complex was
265 rapidly disturbed by LSD1 inhibitors (Maiques-Diaz et al., 2018). Notably, *Gfi1*$^{-/-}$ mice have
266 a near loss of Paneth cells, reduced goblet cell numbers, but more enteroendocrine cells
267 (Shroyer et al., 2005). When we examined genes known to be repressed by GFI1, we found
268 increase of *Neurog3* and *Neurod1*, but not that of mature enteroendocrine cell markers *Chga*
269 and *Chgb* (Fig. 3K, 3L). This is in accordance with equal enteroendocrine cells *in vivo* in WT
270 and KO mice (Fig. 2E, S2F). Together, this suggests that inhibition of LSD1 rapidly leads to
271 de-repression of GFI1-targeted enteroendocrine-progenitor markers, that in turn block PC
272 differentiation, but fail to become fully mature enteroendocrine cells. Additionally, a broad,
273 yet undefined, lack of epithelial maturation would impair PC and enteroendocrine
274 differentiation, which together leads to a complete loss of PCs and equal ChgA^{+} cells in adult
275 intestinal epithelium of KO mice.

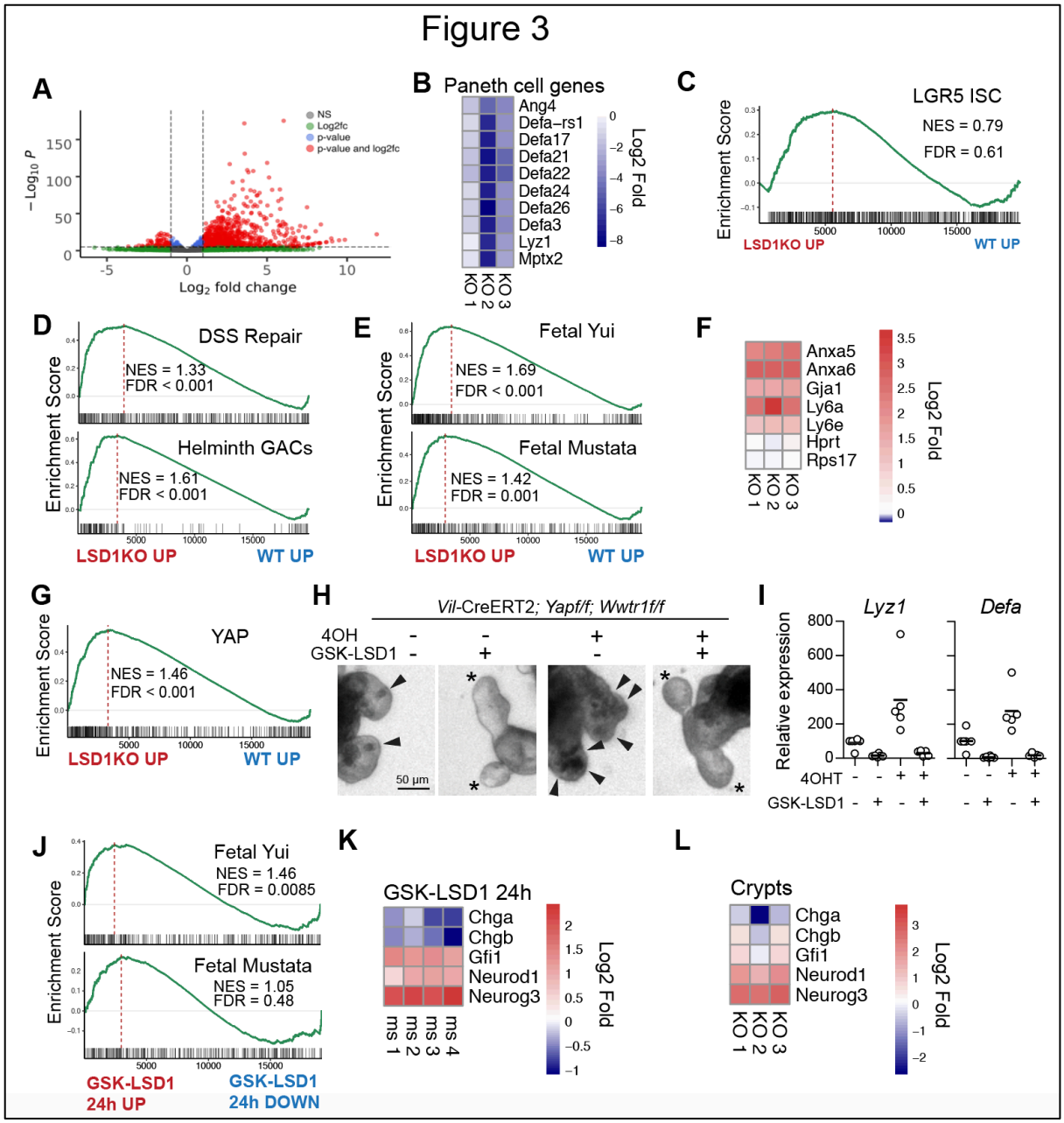

Fig. 3 | Deletion of LSD1 renders intestinal epithelium fetal-like. A, Volcano plot of RNA-seq data comparing WT and KO crypt cells (n=3). **B,** Heatmap of PC-specific genes. **C-E, and G,** LSD1KO *vs.* WT RNA-seq data was analyzed by gene set enrichment analysis (GSEA) for indicated gene signatures. Normalized Enrichment Score (NES) and False Discovery Rates (FDR) are indicated. **F,** Heatmaps of fetal and housekeeping genes from indicated RNA-seq data. **H,** Brightfield images of organoids with indicated treatments. Arrows indicate granular PCs, asterisks indicate crypts devoid of PCs. **I**, Expression of *Lyz1* and *Defa* by qPCR relative to *Actb*, each dot represents a well, pooled from 4 independent experiments. **J,** GSEA analysis of 24 h GSK-LSD1 *vs.* untreated organoid RNA-seq data for indicated gene signatures. **K, L,** Heatmaps of enteroendocrine associated genes from indicated RNA seq data.

LSD1 controls H3K4me1 levels of genes associated with a fetal-like profile

288 LSD1 controls embryonic development by repressing enhancers to allow for embryonic stem
289 cell differentiation (Agarwal et al., 2017; Whyte et al., 2012). We did not observe major
290 differences in global H3K4me1/2 levels by immuno-histochemistry comparing escaper
291 $LSD1^{+}$ crypts in KO tissue (Fig. S4A). To assess if LSD1 mediates H3K4 demethylation
292 and/or chromatin accessibility, we performed ChIP-seq for H3K4me1 and H3K4me2 as well
293 as ATAC-seq comparing sorted WT and KO crypt cells. Analysis of ChIP-seq for H3K4me1
294 identified 2059 sites with associated altered methylation levels, of which the majority (1622)
295 were enriched in KO crypts (Fig. 4A). ChIP-seq of H3K4me2 revealed a very similar pattern
296 and the large majority of genes affected by LSD1 with gain of H3K4me2 were also
297 significant in the analysis for H3K4me1 (Fig. S4B, S4C). In support, analysis of ATAC-seq
298 of sites with differential H3K4me1 levels showed a modest increase in open chromatin (Fig.
299 4A). In addition, most of these peaks are not in close proximity to TSS sites (Fig. S4D). The
300 top 300 genes associated with increased H3K4me1 levels in the KO, are overall enriched in
301 the KO transcriptional profile (Fig. 4B). These include established regenerative markers such
302 as *Ly6a, Ly6e,* and *Anxa6* (Fig. S4E). Analysis of ATAC-seq data identified 864 sites to have
303 more open chromatin of which 608 sites had increased ATAC levels in KO crypt cells and
304 were associated with higher H3K4me1 levels (Fig. 4C). In addition, the majority of genes
305 associated with higher ATAC peaks were upregulated in KO crypts (Fig. S4F). Furthermore,
306 using a high stringency (adj. $p<0.01$), we combined our RNA-seq, ChIP-seq, and ATAC-seq
307 data to find a decent overlap of the genes associated by ChIP, ATAC, or both (Fig. 4D).
308 Because LSD1 demethylates H3K4me1, we assume by combining our H3K4me1 ChIP-seq
309 and RNA-seq data, we establish a core list of 228 genes putatively directly affected by *Lsd1*
310 loss (Fig. 4F, Table S2). Importantly, 84% of the increased H3K4me1 peaks associated with
311 these 228 genes are located outside the 2 kb surrounding the TSS. This suggests that LSD1
312 would drive enhancer-mediated regulation of these genes, which fits with a role generally
313 associated with LSD1 (Agarwal et al., 2017; Whyte et al., 2012). In addition, the LSD1 core
314 signature is enriched in a transcriptional profile comparing fetal with adult organoids (Fig. 4E
315 (Yui et al., 2018)).
316
317 **LSD1 controls genes separately from PRC2**
318 Several groups have shown that EED, an essential component of the Polycomb Repressive
319 Complex 2 (PRC2), is essential for maintaining adult ISCs and crypts, likely by repressing
320 fetal and embryonic genes (Chiacchiera et al., 2016; Jadhav et al., 2019; Koppens et al.,
321 2016). Comparing the LSD1 core with the EED core (genes up in EEDKO crypts and

associated with H3K27me3 peaks (Koppens et al., 2016)) revealed strikingly little overlap between regulated genes (Fig. 4F). Further analysis confirmed that also the majority of putative LSD1-controlled H3K4me1 genes are not 'co-repressed' by the PRC2-mediated H3K27me3 (Fig. S4G). Thus, this suggests that both LSD1 and PRC2 control fetal-like genes but in an unrelated fashion.

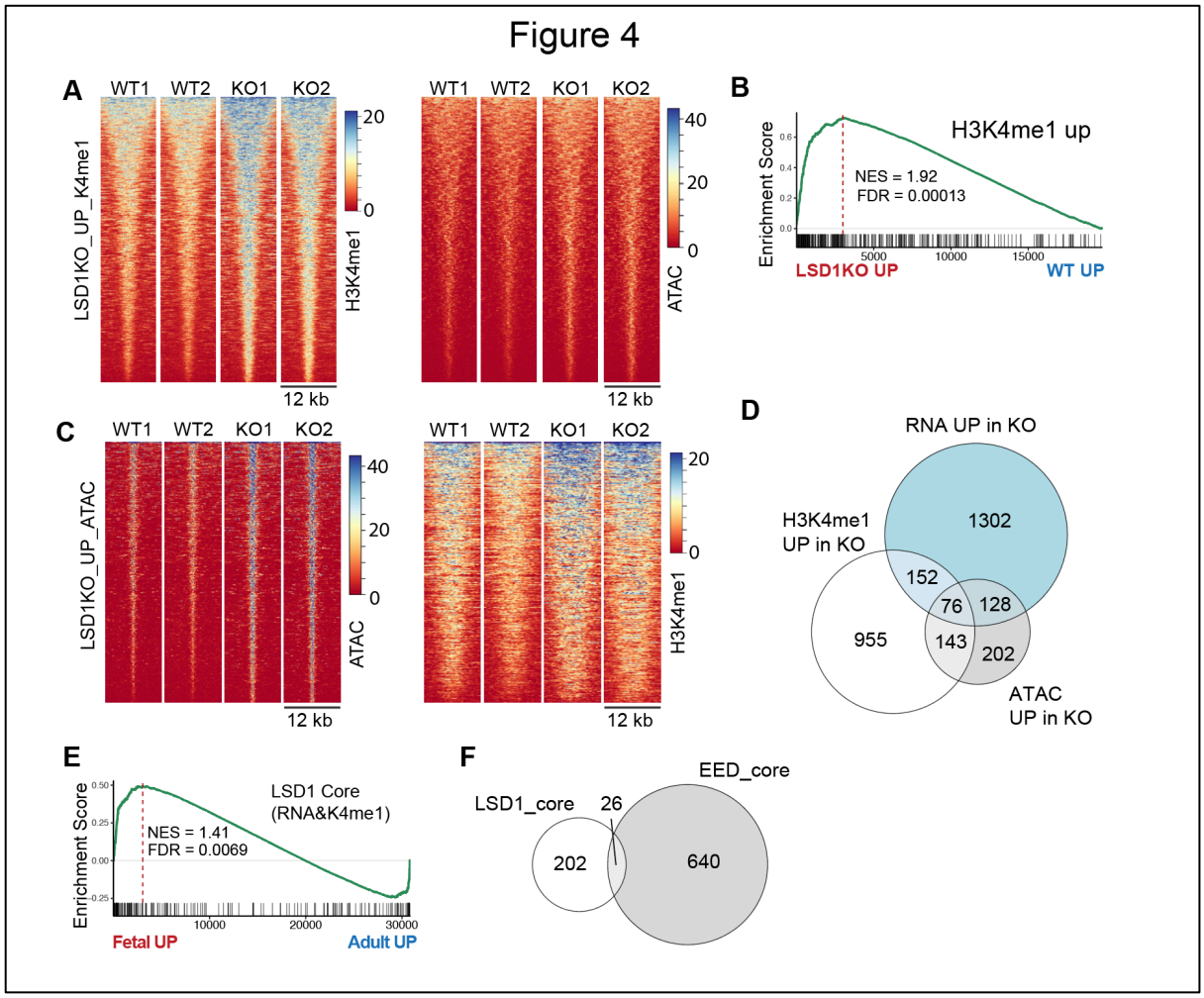

Fig. 4 | LSD1 controls H3K4me1/2 levels of fetal-like genes. A & C, Heatmaps of H3K4me1 (A) and ATAC (C) sites that are significantly up in KO crypts compared to WT crypts. **B,** RNA-seq analysis by GSEA of KO *vs* WT transcriptional profile on a gene set consisting of genes with associated increased H3K4me1 levels in KO crypts. **D,** Venn diagram comparing genes with significant H3K4me1 and ATAC peaks with differential RNA expression (p. adj<0.01). **E,** GSEA of LSD1 core gene list (228 genes) on a transcriptome data set that compares fetal to adult organoids (Yui et al., 2018). **F,** Venn diagram comparing the LSD1 core, and the EED core (genes up in EED KO crypts AND have H3K27me3 associated peak).

Defining fetal and early life gene programs in developing intestinal epithelium

So far, we have found that LSD1 controls postnatal cell lineage differentiation (Fig. 1, 2), which correlates with a fetal-like or reparative gene program (Fig. 3), that in turn may be

339 mediated by the H3K4me1 demethylation role of LSD1 and/or its co-repressive role with
340 other regulators such as GFI1 (Fig. 3, 4). To distinguish fetal from postnatal intestinal
341 epithelial development we performed RNA-seq on embryonic (E) day 18.5, as well as
342 postnatal (P) days 7 and P21 (Fig. S5A, S5B). Figure 5A shows how established cell lineage
343 markers behave during development. As expected, we observed a stepwise increase in ISC
344 markers, an abrupt appearance of PC genes at P21, and goblet and enteroendocrine gene
345 expression at E18.5 and P7 stages that only increases slightly at P21 (Fig. 5A). This indeed
346 supports our hypothesis that KO mice have intestinal epithelium that is 'stuck' at a P7 stage,
347 lacking PCs, with reduced goblet cell and immature enteroendocrine cells, but with crypts
348 containing ISC-like cells. When we compared genes upregulated in KO crypts to different
349 developmental stages we see overlap with both E18.5 and P7 stages compared to P21 (Fig.
350 5B), and, a very similar pattern is noted in EED KO crypts (Fig. 5C). In a separate test, we
351 found enrichment by GSEA for our own fetal (E18vsP7) and neonatal (P7vsP21) gene sets as
352 well as E18 and P7 unique genes (Fig. 5D, S5C). Together, this suggests that both EED and
353 LSD1 control different gene sets throughout intestinal epithelial development in a similar
354 fashion, which results in a striking phenotypical difference: EED KO epithelium returns to a
355 fetal and even embryonic state and mice become moribund (Jadhav et al., 2019), whereas
356 LSD1 KO mice retain an early-life postnatal stage and appear normal up to at least 1 year.
357
358 **Developmental profiles suggest no determining role for LSD1 in H3K4me1**
359 **demethylation for fetal or postnatal specific sites.**
360 To support our transcriptomic analysis, we also performed H3K4me1 ChIP-seq on FACS
361 sorted epithelium at different developmental stages. As an example, we find a robust stepwise
362 increase of H3K4me1 levels near the ISC marker gene *Olfm4*, whereas another ISC marker
363 *Lgr5* has mostly unchanged H3K4me1 levels (Fig. 5E, S5D). When we systemically assess
364 differential sites, we find that there is an abrupt loss of H3K4me1 at P21 from sites that are
365 significantly up in E18.5 and P7 (Fig. 5F, 5G). In contrast, ChIP levels that are low in E18.5
366 or P7 display a stepwise increase that culminates at P21 (Fig. 5F, 5G). Notably, there are
367 fewer peak changes from E18.5 *vs.* P7, compared to P7 *vs.* P21 or E18.5 *vs.* P21 (3700,
368 15522, 26942 significant sites respectively) (Fig. 5F, 5G, S5E). This suggest that the major
369 H3K4me1 transition occurs after P7, which would fit very well with our hypothesis that
370 LSD1 controls this transition specifically. However, when we take these sites and display the
371 H3K4me1 ChIP-seq data of WT *vs.* KO crypts, we find a complete lack of regulation of sites
372 lost at P21 (Fig. 5F, 5G, S5E), nor did we observe increased ATAC levels (data not shown).

373 This suggests that LSD1 is not involved at all in the observed reduction of H3K4me1 sites at
374 P21. In contrast, we observe a modest increase of H3K4me1 levels in KO crypts of the sites
375 that normally culminate at P21 (Fig. 5F, 5G, S5E). In support, if we do the reverse, by taking
376 the significant KO sites from Fig. 4A and display the different developmental stages, we see
377 a stepwise increase of those peaks in time (Fig. S5F). This surprising finding suggests that
378 LSD1 broadly modulates H3K4me1 levels of peaks that appear during development, but that
379 LSD1 is not involved in H3K4me1 sites that are lost during the different developmental
380 stages in intestinal epithelium.
381
382 To test if LSD1 controls other transcriptional regulators, we selected these from the genes
383 upregulated in KO crypts (Egolf et al., 2019; Lambert et al., 2018). We found 73 significantly
384 upregulated transcriptional regulators (Padj<0.01), and many are specifically fetal and/or
385 neonatally expressed, including *Prdm1* (Blimp1) (Fig. 5H, S5G). *Prdm1*KO mice have
386 previously been shown to have increased maturation of the intestinal epithelium, with PCs
387 already present at P7 (Muncan et al., 2011). In addition, many other candidates such as
388 *Arid3a* and several Hoxa family members could be involved in regulating postnatal intestinal
389 epithelial development. Future studies will be directed to test whether any of these have a
390 dominant role.
391

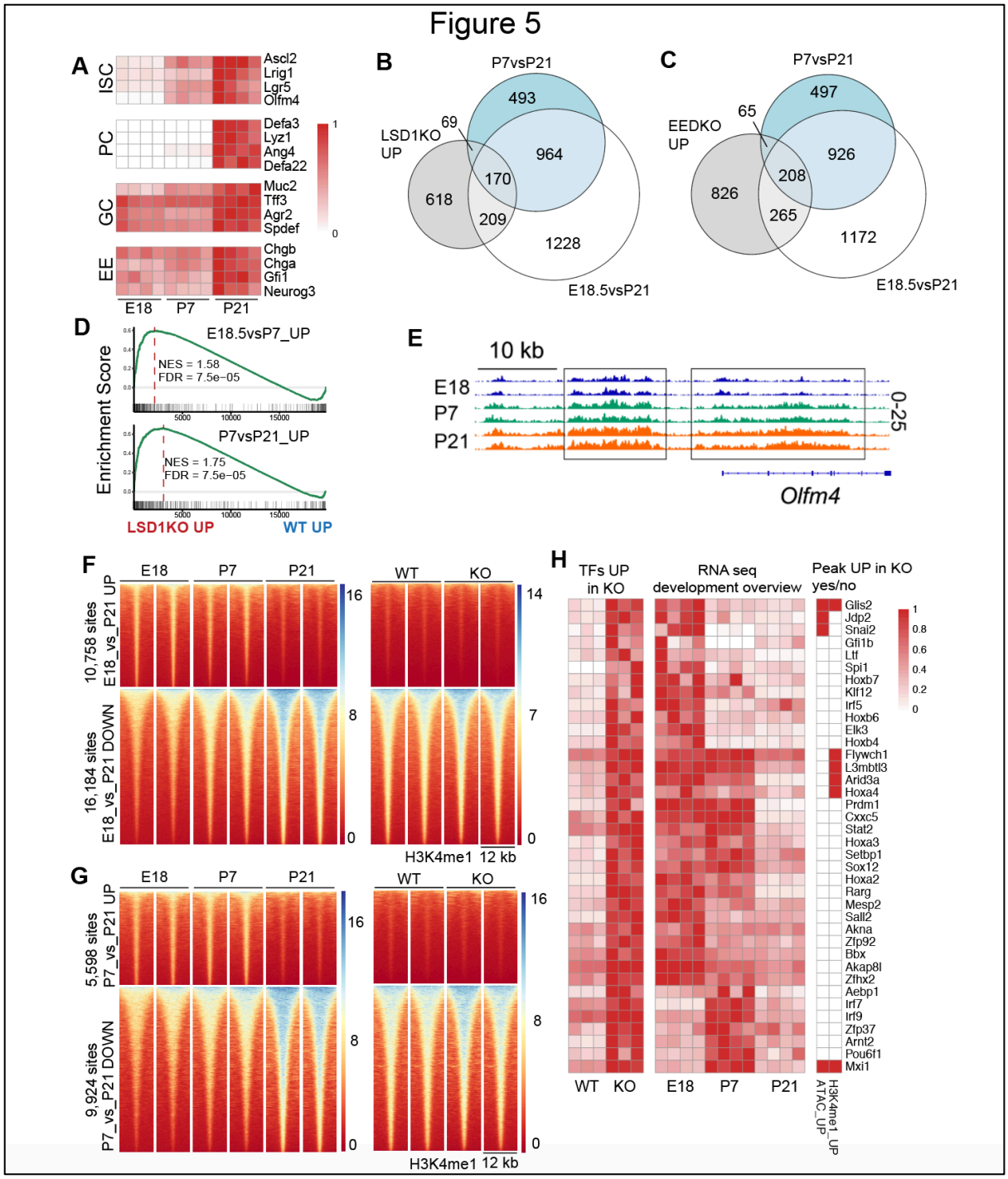

Fig. 5 | LSD1 controls fetal and neonatal genes, but not fetal and neonatal-specific H3K4me1 levels. A, Heatmap of genes associated with ISCs, PCs, goblet cells (GC), and enteroendocrine cells (EE) during development. Shows expression relative to the highest TPM for that gene, which is set to 1. **B&C,** Venn diagram of genes significantly higher expressed in LSD1KO (B) or EEDKO (C) compared with genes that are up in P7*vs.*P21 and E18*vs.*P21. **D,** GSEA of KO *vs.* WT transcriptional profile on fetal (E18*vs.*P7) and neonatal (P7*vs.*P21) gene sets generated from RNA-seq shown in Fig. S5A and S5B. **E,** H3K4me1 profiles of *Olfm4* locus at indicated developmental stages. **F,** Heatmap of H3K4me1 sites that were identified to be significantly higher at E18 (UP) compared to P21 (DOWN) (left panel). Heatmap of WT and KO H3K4me1 profiles of significantly differential sites between E18 and P21 (right panel). **G,** Heatmap of H3K4me1 sites that were

402 identified to be significantly higher at P7 (UP) compared to P21 (DOWN) (left panel). Heatmap of WT and KO
403 H3K4me1 profiles of significantly differential sites between P7 and P21 (right panel). **H,** Heatmaps of
404 transcriptional regulators selected based on upregulation in KO crypts compared to WT crypts. Here are
405 displayed the genes that have either a fetal or a neonatal enrichment, those that have no enrichment or
406 enrichment at P21 are shown in Fig. S5G. On the right is displayed whether there are gene-associated increased
407 ATAC or H3K4me1 ChIP levels in KO crypts.
408

409 **LSD1 expression is downregulated during repair**

410 Based on our data we hypothesize a model in which LSD1 is actively controlled during
411 postnatal epithelial development where first, *de novo* crypt formation is allowed in the
412 absence of LSD1, and afterwards, epithelial maturation (including PC differentiation)
413 requires LSD1. In mice, crypt formation occurs in the first week after birth during
414 development, but also after damage such as upon radiation injury. Therefore, we studied
415 LSD1 expression after whole body irradiation (10 gy) and found that LSD1 is much lower
416 expressed in regenerating epithelium 3 days post irradiation, compared to naïve mice (Fig.
417 6A). Of note, this is near opposite of the Hippo-transducer YAP expression pattern (Fig.
418 S6A). In support, we assessed *Lsd1* expression in a recently described single cell RNA-seq
419 experiment comparing crypt cells during homeostasis and during active repair (Ayyaz et al.,
420 2019), and found a clear reduction in number of crypt cells expressing *Lsd1* (Fig. 6B). In
421 summary, *Lsd1* is actively downregulated during crypt formation both in developing as well
422 as repairing intestines.
423

424 ***Lsd1*-deficient epithelium has superior reparative capacity**

425 We found that genetic loss of *Lsd1 in vivo* or LSD1 inhibition *in vitro* leads to intestinal
426 epithelium with neonatal and/or repairing features. This prompted us to test whether a
427 'reparative' state during homeostasis would be beneficial after injury. We irradiated WT and
428 KO mice with 10 Gy and we did not observe pathological differences 6 days post treatment
429 (Fig. 6C, S6B). However, we did find an increase in crypt length 3 days after injury, as
430 measured by Ki67^{+} (Fig. 6D, 6E). We found no evidence of appearing PCs after injury in KO
431 tissue (Fig. 6F). We did find that the Olfm4^{+} ISC zone similarly expanded as the Ki67^{+} crypts
432 (Fig. 6D, 6F). We next irradiated mice with 16 Gy, when WT mice are unable to recover by
433 day 6, in contrast, KO epithelium regained crypt-villus structures and had lower pathology
434 scores compared to WT epithelium (Fig. 6H, 6I, S6C, S6D). Thus, KO epithelial tissue that
435 have a pre-existing repairing profile enhances repair *in vivo* after radiation injury.
436

437 Finally, we performed a gene expression array of GSK-LSD1 treated human organoids, and
438 found that the LSD1 core and a fetal signature were enriched in GSK-LSD1 treated human
439 organoids (Fig. 6J).
440
441 In summary, we provide evidence that inhibition of LSD1 may be a viable target for the
442 reprogramming of intestinal epithelium into a reparative state that is beneficial after injury,
443 such as inflicted by radiation therapy.

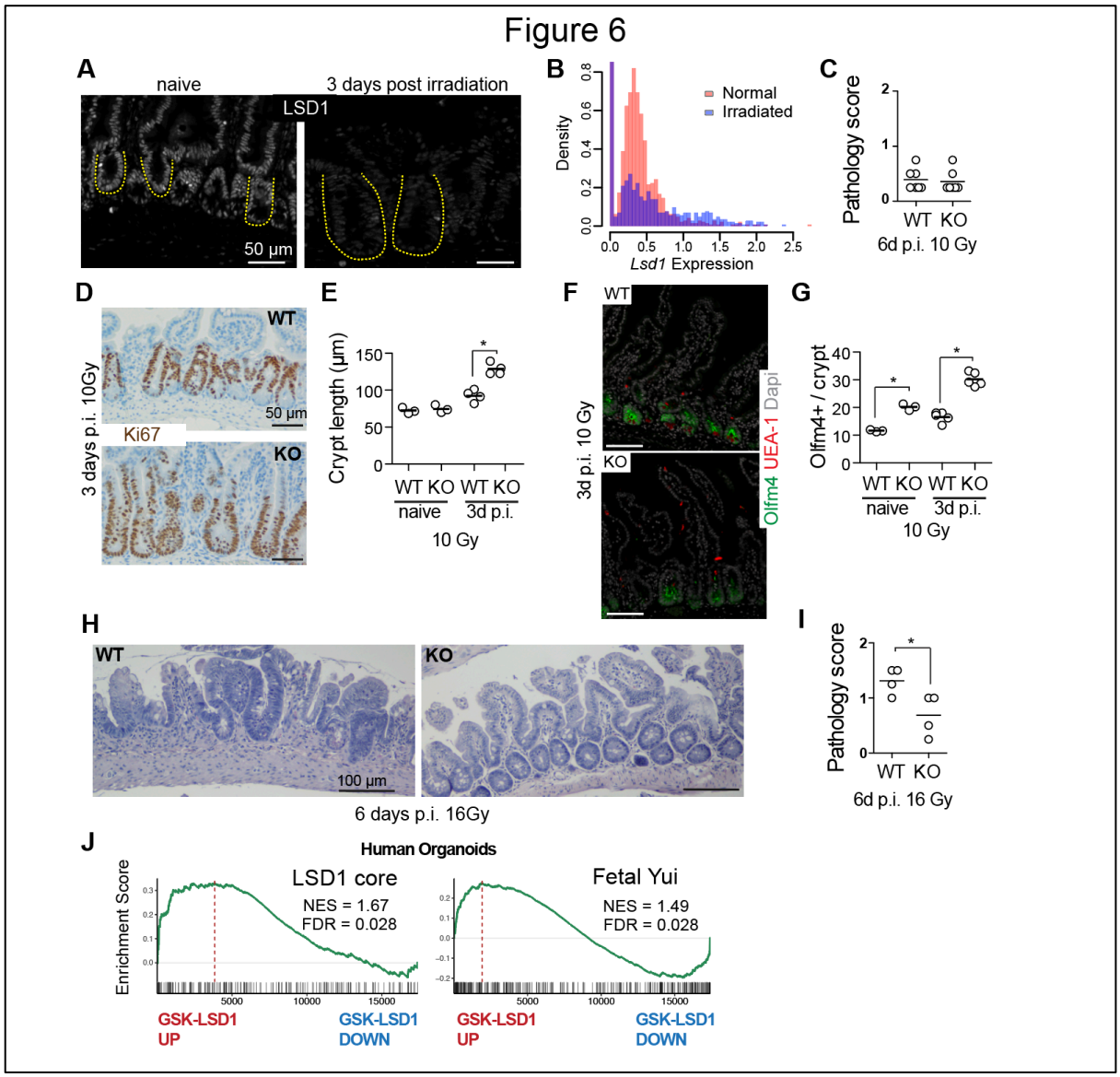

444
445 **Fig. 6 | LSD1 levels are actively reduced during repair and *Lsd1*-deficient epithelium repairs better than**
446 **WT tissue. A,** Images of LSD1 antibody staining of naïve and irradiated (10 gy) intestines. **B,** *Lsd1* expression
447 from single-cell RNA-seq data from (Ayyaz et al., 2019) in normal and irradiated crypts. **C,** Pathology score of
448 indicated intestines 6 days post irradiation (p.i.) with 10 Gy. **D,** Images of Ki67 antibody staining of WT and
449 KO tissue 3 days p.i.. **E,** Crypt length as quantified from images shown in 6D and S2H, crypt length is
450 determined by Ki67^{+} cells. **F,** Images of Olfm4, UEA-1, and Dapi stained WT and KO intestines 3 days p.i. at

10 Gy. **G,** Quantifications of Olfm4$^+$ cells per crypt quantified from images such as shown in 6F and 2G. **H,** H&E staining of WT and KO intestinal tissue 6 days p.i. with 16 Gy. **I,** Pathology score of indicated intestines 6 days p.i. with 16 Gy. **J,** GSEA of indicated signatures on transcriptome data generated from control and GSK-LSD1 treated human organoids. * $p<0.05$

DISCUSSION

In this study, we show that spatiotemporal regulation of LSD1 occurs in the developing intestine and during repair, and that LSD1 is important for crypt maturation, which includes the appearance of PCs. Notably, while LSD1 KO mice fail to develop any PCs, organoids derived from KO epithelium are formed and normally maintained, even in the absence of Wnt. Although these resemble organoids derived from fetal epithelium that also lack PCs (Fordham et al., 2013; Mustata et al., 2013), there are some key distinctions. Unlike fetal organoids, KO organoids cannot grow without R-spondin 1 (Fig. 3F). In addition, KO organoids form crypts, likely because Notch-ligand expressing cells required for 'symmetry breaking' are still present (Serra et al., 2019), such as enteroendocrine progenitors (van Es et al., 2019). In contrast, fetal organoids remain spheroid, and only form crypts after a 'maturation' trigger, at which point they also lose the ability to grow without R-spondin 1. Our data suggests that KO organoids would be in between fetal and adult, having features of both; not relying on Wnt yet unable to grow without R-spondin 1.

Intestinal epithelial repair is crucial to prevent chronic disease, and YAP/TAZ are established initiators and critical regulators of this process (Cai et al., 2010; Gregorieff et al., 2015; Yui et al., 2018). YAP/TAZ are sensors of mechanical signals (Dupont et al., 2011), so it is plausible that upon damage, and subsequent ECM cues, YAP/TAZ are activated by control of their protein levels (Cai et al., 2010; Yui et al., 2018). We found a clear reduction of LSD1 levels after irradiation, which coincides with an increase in YAP levels. Although it is unclear how LSD1 levels are controlled after regeneration, in glioblastoma tumor cells GSK3β stabilizes LSD1 by direct phosphorylation (Zhou et al., 2016). Thus, activation of the Wnt pathway, which occurs during the regenerating phase, could lead to fast reduction of LSD1 levels by Wnt-controlled inhibition of GSK3. We further found that LSD1 represses a reparative gene expression profile, similar to that activated by YAP. However, GSK-LSD1-mediated depletion of PCs was completely independent of YAP/TAZ (Fig. 3H, 3I). In combination, after damage, reducing levels of the repressor LSD1, and inducing levels of activators YAP/TAZ, can together mediate a robust reparative response.

485

486 Maintenance of chromatin accessibility is required for intestinal physiology, for example by
487 DNA methylation (D.-H. Yu et al., 2015). In addition, three groups have independently
488 identified a crucial role for the PRC2 complex in intestinal epithelial biology (Chiacchiera et
489 al., 2016; Jadhav et al., 2019; 2016; Koppens et al., 2016). In 2019, Jadhav et al. proposes a
490 model in which, upon deletion of PRC2 member EED, first fetal and subsequent embryonic
491 genes are re-activated in adult epithelium (Jadhav et al., 2019). This initially leads to loss of
492 ISCs and aberrant differentiation, and ultimately leads to loss of structure and moribund mice
493 14 days after deletion of EED (Jadhav et al., 2019). When we compared EED core genes
494 (genes up in EED KO crypts combined with H3K27me3 associated genes) with LSD1 core
495 genes (up in LSD1 KO, and increase H3K4me1 levels in LSD1 KO) we found very little
496 overlap, suggesting that there are not many genes co-repressed by PRC2 and LSD1
497 complexes, which would explain the difference in severity of their KO phenotypes.
498 Surprisingly, LSD1 does not control H3K4me1 sites that are specific for E18 or P7
499 developmental stages (Fig. 5F, 5G). This is in stark contrast to PRC2 controlled sites that are
500 primarily fetal and embryonic (Jadhav et al., 2019). Nonetheless, putative LSD1-controlled
501 genes include those associated with altered H3K4me1 levels in KO crypts, as well as genes
502 that may be regulated independently of LSD1 demethylase activity, such as those being co-
503 repressed by GFI1 (Fig. 3K, 3L) (Maiques-Diaz et al., 2018). In addition, we present a list of
504 transcriptional regulators with increased expression in LSD1 KO crypts, including previously
505 identified regulator of intestinal epithelial development PRDM1 (BLIMP-1) (Muncan et al.,
506 2011). Together, we conclude that LSD1 controls fetal and neonatal genes but in a rapid
507 reversible fashion where cells retain their ability to mature, which happens either between P7-
508 P21 or after injury, making LSD1 an attractive targeting candidate for stimulating intestinal
509 repair in patients. Future studies will be directed towards identifying the specific regulatory
510 mechanisms driving the repression of fetal and neonatal genes in adult intestinal epithelium
511 by LSD1.
512

513 **ACKNOWLEDGEMENTS**

514 We kindly thank Colby Zaph for the initial support of this study and critical reading of the
515 manuscript. We thank Unni Nonstad for assistance with cell sorting. We are indebted to Anne
516 Marthinsen for performing the irradiation after working hours, and the Department of
517 Radiology and Nuclear Medicine (St. Olavs Hospital) for allowing the use of their
518 instruments. We thank the imaging (CMIC) and animal care (CoMed) core facilities that

assisted in this work (NTNU). The WT KO crypt RNA-seq was done by the Genomics Core Facility at NTNU, which receives funding from the Faculty of Medicine and Health Sciences and Central Norway Regional Health Authority. The ChIP sequencing was done at the Norwegian Sequencing Centre (www.sequencing.uio.no), a national technology platform hosted by the University of Oslo and supported by the "Functional Genomics" and "Infrastructure" programs of the Research Council of Norway and the Southeastern Regional Health Authorities. Funding of this work was provided by the Norwegian Research Council (Centre of Excellence grant 223255/F50, and 'Young Research Talent' 274760 to MJO) and the Norwegian Cancer Society (182767 to MJO). MMA is the recipient of a Marie Skłodowska-Curie IF (DLV-794391). This work was also supported by the South-Eastern Norway Regional Health Authority, Early Career Grant 2016058, and the Research Council of Norway "Young Research Talent" grant to JAD. MF is supported by the Norwegian Research Council (grant no. 275286). The SGC is a registered charity (number 1097737) that receives funds from AbbVie, Bayer Pharma AG, Boehringer Ingelheim, Canada Foundation for Innovation, Eshelman Institute for Innovation, Genome Canada through Ontario Genomics Institute [OGI-055], Innovative Medicines Initiative (EU/EFPIA) [ULTRA-DD grant no. 115766], Janssen, Merck KGaA, Darmstadt, Germany, MSD, Novartis Pharma AG, Ontario Ministry of Research, Innovation and Science (MRIS), Pfizer, São Paulo Research Foundation-FAPESP, Takeda, and Wellcome. This project also received funding from the European Union's Horizon 2020 research and innovation programme (grant agreements INTENS 668294, MTP, KBJ). The Novo Nordisk Foundation Center for Stem Cell Biology is supported by a Novo Nordisk Foundation grant number NNF17CC0027852 (KBJ).

Author contributions: R.T.Z., H.T.L., M.F., M.T.P., Y.O., A.D.S, M.M.A., J.O., M.M., N.P., E.K., R.R.S., and M.J.O. performed experiments. K.N. and C.A. provided essential reagents. M.R., F.D., C.A., J.A.D., K.B.J., T.S., and M.J.O. supervised and/or provided conceptual insight. M.J.O wrote a first draft with subsequent input from all authors.

Competing interests: T.S. is an inventor on several patents related to organoid culture.

Correspondence and request for materials should be addressed to M.J.O.

REFERENCES

553 Agarwal, S., Garay, P.M., Porter, R.S., Brookes, E., Murata-Nakamura, Y., Macfarlan, T.S.,
554 Ren, B., Iwase, S., 2017. LSD1/KDM1A Maintains Genome-wide Homeostasis of
555 Transcriptional Enhancers 1–39. doi:10.1101/146357
556 Ayyaz, A., Kumar, S., Sangiorgi, B., Ghoshal, B., Gosio, J., Ouladan, S., Fink, M., Barutcu,
557 S., Trcka, D., Shen, J., Chan, K., Wrana, J.L., Gregorieff, A., 2019. Single-cell
558 transcriptomes of the regenerating intestine reveal a revival stem cell. Nature 569, 121–
559 125. doi:10.1038/s41586-019-1154-y
560 Azzolin, L., Panciera, T., Soligo, S., Enzo, E., Bicciato, S., Dupont, S., Bresolin, S., Frasson,
561 C., Basso, G., Guzzardo, V., Fassina, A., Cordenonsi, M., Piccolo, S., 2014. YAP/TAZ
562 Incorporation in the β-Catenin Destruction Complex Orchestrates the Wnt Response. Cell
563 158, 157–170. doi:10.1016/j.cell.2014.06.013
564 Barker, N., van Es, J.H., Kuipers, J., Kujala, P., van den Born, M., Cozijnsen, M.,
565 Haegebarth, A., Korving, J., Begthel, H., Peters, P.J., Clevers, H., 2007. Identification of
566 stem cells in small intestine and colon by marker gene Lgr5. Nature 449, 1003–1007.
567 doi:10.1038/nature06196
568 Bastide, P., Darido, C., Pannequin, J., Kist, R., Robine, S., Marty-Double, C., Bibeau, F.,
569 Scherer, G., Joubert, D., Hollande, F., Blache, P., Jay, P., 2007. Sox9 regulates cell
570 proliferation and is required for Paneth cell differentiation in the intestinal epithelium. J
571 Cell Biol 178, 635–648. doi:10.1083/jcb.200704152
572 Buczacki, S.J.A., Zecchini, H.I., Nicholson, A.M., Russell, R., Vermeulen, L., Kemp, R.,
573 Winton, D.J., 2013. Intestinal label-retaining cells are secretory precursors expressing
574 lgr5. Nature 495, 65–69. doi:10.1038/nature11965
575 Cai, J., Zhang, N., Zheng, Y., de Wilde, R.F., Maitra, A., Pan, D., 2010. The Hippo signaling
576 pathway restricts the oncogenic potential of an intestinal regeneration program. Genes
577 Dev. 24, 2383–2388. doi:10.1101/gad.1978810
578 Chiacchiera, F., Rossi, A., Jammula, S., Zanotti, M., Pasini, D., 2016. PRC2 preserves
579 intestinal progenitors and restricts secretory lineage commitment. Embo J 35, 2301–
580 2314. doi:10.15252/embj.201694550
581 Degirmenci, B., Valenta, T., Dimitrieva, S., Hausmann, G., Basler, K., 2018. GLI1-
582 expressing mesenchymal cells form the essential Wnt-secreting niche for colon stem
583 cells. Nature 558, 449–453. doi:10.1038/s41586-018-0190-3
584 Dupont, S., Morsut, L., Aragona, M., Enzo, E., Giulitti, S., Cordenonsi, M., Zanconato, F., Le
585 Digabel, J., Forcato, M., Bicciato, S., Elvassore, N., Piccolo, S., 2011. Role of YAP/TAZ
586 in mechanotransduction. Nature 474, 179–183. doi:10.1038/nature10137
587 Durand, A., Donahue, B., Peignon, G., Letourneur, F., Cagnard, N., Slomianny, C., Perret,
588 C., Shroyer, N.F., Romagnolo, B., 2012. Functional intestinal stem cells after Paneth cell
589 ablation induced by the loss of transcription factor Math1 (Atoh1). Proc Natl Acad Sci U
590 S A 109, 8965–8970. doi:10.1073/pnas.1201652109
591 Egolf, S., Aubert, Y., Doepner, M., Anderson, A., Maldonado-Lopez, A., Pacella, G., Lee, J.,
592 Ko, E.K., Zou, J., Lan, Y., Simpson, C.L., Ridky, T., Capell, B.C., 2019. LSD1
593 Inhibition Promotes Epithelial Differentiation through Derepression of Fate-Determining
594 Transcription Factors. CellReports 28, 1981–1992.e7. doi:10.1016/j.celrep.2019.07.058
595 Farin, H.F., van Es, J.H., Clevers, H., 2012. Redundant sources of Wnt regulate intestinal
596 stem cells and promote formation of Paneth cells. Gastroenterology 143, 1518–1529.e7.
597 doi:10.1053/j.gastro.2012.08.031
598 Fordham, R.P., Yui, S., Hannan, N.R.F., Soendergaard, C., Madgwick, A., Schweiger, P.J.,
599 Nielsen, O.H., Vallier, L., Pedersen, R.A., Nakamura, T., Watanabe, M., Jensen, K.B.,
600 2013. Transplantation of expanded fetal intestinal progenitors contributes to colon
601 regeneration after injury. Cell Stem Cell 13, 734–744. doi:10.1016/j.stem.2013.09.015

602 Fujii, M., Matano, M., Toshimitsu, K., Takano, A., Mikami, Y., Nishikori, S., Sugimoto, S.,
603 Sato, T., 2018. Human Intestinal Organoids Maintain Self-Renewal Capacity and
604 Cellular Diversity in Niche-Inspired Culture Condition. Cell Stem Cell 23, 787–793.e6.
605 doi:10.1016/j.stem.2018.11.016
606 Gregorieff, A., Liu, Y., Inanlou, M.R., Khomchuk, Y., Wrana, J.L., 2015. Yap-dependent
607 reprogramming of Lgr5(+) stem cells drives intestinal regeneration and cancer. Nature
608 526, 715–718. doi:10.1038/nature15382
609 Greicius, G., Kabiri, Z., Sigmundsson, K., Liang, C., Bunte, R., Singh, M.K., Virshup, D.M.,
610 2018. PDGFRα $^{+}$ pericryptal stromal cells are the critical source of Wnts and RSPO3 for
611 murine intestinal stem cells in vivo. Proc Natl Acad Sci U S A 115, E3173–E3181.
612 doi:10.1073/pnas.1713510115
613 Guiu, J., Hannezo, E., Yui, S., Demharter, S., Ulyanchenko, S., Maimets, M., Jørgensen, A.,
614 Perlman, S., Lundvall, L., Mamsen, L.S., Larsen, A., Olesen, R.H., Andersen, C.Y.,
615 Thuesen, L.L., Hare, K.J., Pers, T.H., Khodosevich, K., Simons, B.D., Jensen, K.B.,
616 2019. Tracing the origin of adult intestinal stem cells. Nature Publishing Group 154,
617 274–111. doi:10.1038/s41586-019-1212-5
618 Haber, A.L., Biton, M., Rogel, N., Herbst, R.H., Shekhar, K., Smillie, C., Burgin, G.,
619 Delorey, T.M., Howitt, M.R., Katz, Y., Tirosh, I., Beyaz, S., Dionne, D., Zhang, M.,
620 Raychowdhury, R., Garrett, W.S., Rozenblatt-Rosen, O., Shi, H.N., Yilmaz, O., Xavier,
621 R.J., Regev, A., 2017. A single-cell survey of the small intestinal epithelium. Nature 551,
622 333–339. doi:10.1038/nature24489
623 Ho, L.-L., Sinha, A., Verzi, M., Bernt, K.M., Armstrong, S.A., Shivdasani, R.A., 2013.
624 DOT1L-mediated H3K79 methylation in chromatin is dispensable for Wnt pathway-
625 specific and other intestinal epithelial functions. Mol Cell Biol 33, 1735–1745.
626 doi:10.1128/MCB.01463-12
627 Jadhav, U., Cavazza, A., Banerjee, K.K., Xie, H., O'Neill, N.K., Saenz-Vash, V., Herbert, Z.,
628 Madha, S., Orkin, S.H., Zhai, H., Shivdasani, R.A., 2019. Extensive Recovery of
629 Embryonic Enhancer and Gene Memory Stored in Hypomethylated Enhancer DNA. Mol
630 Cell 74, 542–554.e5. doi:10.1016/j.molcel.2019.02.024
631 Jadhav, U., Nalapareddy, K., Saxena, M., O'Neill, N.K., Pinello, L., Yuan, G.-C., Orkin,
632 S.H., Shivdasani, R.A., 2016. Acquired Tissue-Specific Promoter Bivalency Is a Basis
633 for PRC2 Necessity in Adult Cells. Cell 165, 1389–1400. doi:10.1016/j.cell.2016.04.031
634 Jadhav, U., Saxena, M., O'Neill, N.K., Saadatpour, A., Yuan, G.-C., Herbert, Z., Murata, K.,
635 Shivdasani, R.A., 2017. Dynamic Reorganization of Chromatin Accessibility Signatures
636 during Dedifferentiation of Secretory Precursors into Lgr5+ Intestinal Stem Cells. Cell
637 Stem Cell 21, 65–77.e5. doi:10.1016/j.stem.2017.05.001
638 Kerenyi, M.A., Shao, Z., Hsu, Y.-J., Guo, G., Luc, S., O'Brien, K., Fujiwara, Y., Peng, C.,
639 Nguyen, M., Orkin, S.H., 2013. Histone demethylase Lsd1 represses hematopoietic stem
640 and progenitor cell signatures during blood cell maturation. Elife 2, e00633.
641 doi:10.7554/eLife.00633
642 Kim, T.-H., Escudero, S., Shivdasani, R.A., 2012. Intact function of Lgr5 receptor-expressing
643 intestinal stem cells in the absence of Paneth cells. Proc Natl Acad Sci U S A 109, 3932–
644 3937. doi:10.1073/pnas.1113890109
645 Kim, T.-H., Li, F., Ferreiro-Neira, I., Ho, L.-L., Luyten, A., Nalapareddy, K., Long, H.,
646 Verzi, M., Shivdasani, R.A., 2014. Broadly permissive intestinal chromatin underlies
647 lateral inhibition and cell plasticity. Nature 506, 511–515. doi:10.1038/nature12903
648 Koppens, M.A.J., Bounova, G., Gargiulo, G., Tanger, E., Janssen, H., Cornelissen-Steijger,
649 P., Blom, M., Song, J.-Y., Wessels, L.F.A., van Lohuizen, M., 2016. Deletion of
650 Polycomb Repressive Complex 2 From Mouse Intestine Causes Loss of Stem Cells.
651 Gastroenterology 151, 684–697.e12. doi:10.1053/j.gastro.2016.06.020

652 Lambert, S.A., Jolma, A., Campitelli, L.F., Das, P.K., Yin, Y., Albu, M., Chen, X., Taipale,
653 J., Hughes, T.R., Weirauch, M.T., 2018. The Human Transcription Factors. Cell 172,
654 650–665. doi:10.1016/j.cell.2018.01.029
655 Maiques-Diaz, A., Spencer, G.J., Lynch, J.T., Ciceri, F., Williams, E.L., Amaral, F.M.R.,
656 Wiseman, D.H., Harris, W.J., Li, Y., Sahoo, S., Hitchin, J.R., Mould, D.P., Fairweather,
657 E.E., Waszkowycz, B., Jordan, A.M., Smith, D.L., Somervaille, T.C.P., 2018. Enhancer
658 Activation by Pharmacologic Displacement of LSD1 from GFI1 Induces Differentiation
659 in Acute Myeloid Leukemia. CellReports 22, 3641–3659.
660 doi:10.1016/j.celrep.2018.03.012
661 Mohammad, H.P., Smitheman, K.N., Kamat, C.D., Soong, D., Federowicz, K.E., Van Aller,
662 G.S., Schneck, J.L., Carson, J.D., Liu, Y., Butticello, M., Bonnette, W.G., Gorman, S.A.,
663 Degenhardt, Y., Bai, Y., McCabe, M.T., Pappalardi, M.B., Kasparec, J., Tian, X.,
664 McNulty, K.C., Rouse, M., McDevitt, P., Ho, T., Crouthamel, M., Hart, T.K., Concha,
665 N.O., McHugh, C.F., Miller, W.H., Dhanak, D., Tummino, P.J., Carpenter, C.L.,
666 Johnson, N.W., Hann, C.L., Kruger, R.G., 2015. A DNA Hypomethylation Signature
667 Predicts Antitumor Activity of LSD1 Inhibitors in SCLC. Cancer Cell 28, 57–69.
668 doi:10.1016/j.ccell.2015.06.002
669 Muncan, V., Heijmans, J., Krasinski, S.D., Büller, N.V., Wildenberg, M.E., Meisner, S.,
670 Radonjic, M., Stapleton, K.A., Lamers, W.H., Biemond, I., van den Bergh Weerman,
671 M.A., O'Carroll, D., Hardwick, J.C., Hommes, D.W., van den Brink, G.R., 2011. Blimp1
672 regulates the transition of neonatal to adult intestinal epithelium. Nat Commun 2, 1–9.
673 doi:10.1038/ncomms1463
674 Muñoz, J., Stange, D.E., Schepers, A.G., van de Wetering, M., Koo, B.-K., Itzkovitz, S.,
675 Volckmann, R., Kung, K.S., Koster, J., Radulescu, S., Myant, K., Versteeg, R., Sansom,
676 O.J., van Es, J.H., Barker, N., van Oudenaarden, A., Mohammed, S., Heck, A.J.R.,
677 Clevers, H., 2012. The Lgr5 intestinal stem cell signature: robust expression of proposed
678 quiescent "+4" cell markers. Embo J 31, 3079–3091. doi:10.1038/emboj.2012.166
679 Mustata, R.C., Vasile, G., Fernandez-Vallone, V., Strollo, S., Lefort, A., Libert, F.,
680 Monteyne, D., Pérez-Morga, D., Vassart, G., Garcia, M.-I., 2013. Identification of Lgr5-
681 Independent Spheroid-Generating Progenitors of the Mouse Fetal Intestinal Epithelium.
682 Cell Rep 5, 421–432. doi:10.1016/j.celrep.2013.09.005
683 Nusse, Y.M., Nusse, Y.M., Savage, A.K., Savage, A.K., Marangoni, P., Marangoni, P.,
684 Rosendahl-Huber, A.K.M., Rosendahl-Huber, A.K.M., Landman, T.A., Landman, T.A.,
685 de Sauvage, F.J., Locksley, R.M., Klein, O.D., 2018. Parasitic helminths induce fetal-like
686 reversion in the intestinal stem cell niche. Nature 559, 109–113. doi:10.1038/s41586-
687 018-0257-1
688 Sato, T., van Es, J.H., Snippert, H.J., Stange, D.E., Vries, R.G., van den Born, M., Barker, N.,
689 Shroyer, N.F., van de Wetering, M., Clevers, H., 2011. Paneth cells constitute the niche
690 for Lgr5 stem cells in intestinal crypts. Nature 469, 415–418. doi:10.1038/nature09637
691 Sato, T., Vries, R.G., Snippert, H.J., van de Wetering, M., Barker, N., Stange, D.E., van Es,
692 J.H., Abo, A., Kujala, P., Peters, P.J., Clevers, H., 2009. Single Lgr5 stem cells build
693 crypt-villus structures in vitro without a mesenchymal niche. Nature 459, 262–265.
694 doi:10.1038/nature07935
695 Scheer, S., Ackloo, S., Medina, T.S., Schapira, M., Li, F., Ward, J.A., Lewis, A.M.,
696 Northrop, J.P., Richardson, P.L., Kaniskan, H.Ü., Shen, Y., Liu, J., Smil, D., McLeod,
697 D., Zepeda-Velazquez, C.A., Luo, M., Jin, J., Barsyte-Lovejoy, D., Huber, K.V.M.,
698 Carvalho, D.D., Vedadi, M., Zaph, C., Brown, P.J., Arrowsmith, C.H., 2018. A chemical
699 biology toolbox to study protein methyltransferases and epigenetic signaling. Nat
700 Commun 10, 1–14. doi:10.1038/s41467-018-07905-4

701 Serra, D., Mayr, U., Boni, A., Lukonin, I., Rempfler, M., Challet Meylan, L., Stadler, M.B.,
702 Strnad, P., Papasaikas, P., Vischi, D., Waldt, A., Roma, G., Liberali, P., 2019. Self-
703 organization and symmetry breaking in intestinal organoid development. Nature 569, 66–
704 72. doi:10.1038/s41586-019-1146-y
705 Shoshkes-Carmel, M., Wang, Y.J., Wangensteen, K.J., Tóth, B., Kondo, A., Massassa, E.E.,
706 Itzkovitz, S., Kaestner, K.H., 2018. Subepithelial telocytes are an important source of
707 Wnts that supports intestinal crypts. Nature 557, 242–246. doi:10.1038/s41586-018-
708 0084-4
709 Shroyer, N.F., Wallis, D., Venken, K.J.T., Bellen, H.J., Zoghbi, H.Y., 2005. Gfi1 functions
710 downstream of Math1 to control intestinal secretory cell subtype allocation and
711 differentiation. Genes Dev. 19, 2412–2417. doi:10.1101/gad.1353905
712 Tetteh, P.W., Basak, O., Farin, H.F., Wiebrands, K., Kretzschmar, K., Begthel, H., van den
713 Born, M., Korving, J., de Sauvage, F., van Es, J.H., van Oudenaarden, A., Clevers, H.,
714 2016. Replacement of Lost Lgr5-Positive Stem Cells through Plasticity of Their
715 Enterocyte-Lineage Daughters. Cell Stem Cell 18, 203–213.
716 doi:10.1016/j.stem.2016.01.001
717 van Es, J.H., Sato, T., van de Wetering, M., Lyubimova, A., Yee Nee, A.N., Gregorieff, A.,
718 Sasaki, N., Zeinstra, L., van den Born, M., Korving, J., Martens, A.C.M., Barker, N., van
719 Oudenaarden, A., Clevers, H., 2012. Dll1+ secretory progenitor cells revert to stem cells
720 upon crypt damage. Nat Cell Biol 14, 1099–1104. doi:10.1038/ncb2581
721 van Es, J.H., Wiebrands, K., López-Iglesias, C., van de Wetering, M., Zeinstra, L., van den
722 Born, M., Korving, J., Sasaki, N., Peters, P.J., van Oudenaarden, A., Clevers, H., 2019.
723 Enteroendocrine and tuft cells support Lgr5 stem cells on Paneth cell depletion. Proc Natl
724 Acad Sci U S A 31, 201801888–26605. doi:10.1073/pnas.1801888117
725 Whyte, W.A., Bilodeau, S., Orlando, D.A., Hoke, H.A., Frampton, G.M., Foster, C.T.,
726 Cowley, S.M., Young, R.A., 2012. Enhancer decommissioning by LSD1 during
727 embryonic stem cell differentiation. Nature 482, 221–225. doi:10.1038/nature10805
728 Yan, K.S., Gevaert, O., Zheng, G.X.Y., Anchang, B., Probert, C.S., Larkin, K.A., Davies,
729 P.S., Cheng, Z.-F., Kaddis, J.S., Han, A., Roelf, K., Calderon, R.I., Cynn, E., Hu, X.,
730 Mandleywala, K., Wilhelmy, J., Grimes, S.M., Corney, D.C., Boutet, S.C., Terry, J.M.,
731 Belgrader, P., Ziraldo, S.B., Mikkelsen, T.S., Wang, F., Furstenberg, von, R.J., Smith,
732 N.R., Chandrakesan, P., May, R., Chrissy, M.A.S., Jain, R., Cartwright, C.A., Niland,
733 J.C., Hong, Y.-K., Carrington, J., Breault, D.T., Epstein, J., Houchen, C.W., Lynch, J.P.,
734 Martin, M.G., Plevritis, S.K., Curtis, C., Ji, H.P., Li, L., Henning, S.J., Wong, M.H., Kuo,
735 C.J., 2017. Intestinal Enteroendocrine Lineage Cells Possess Homeostatic and Injury-
736 Inducible Stem Cell Activity. Cell Stem Cell 21, 78–90.e6.
737 doi:10.1016/j.stem.2017.06.014
738 Yang, Q., Bermingham, N.A., Finegold, M.J., Zoghbi, H.Y., 2001. Requirement of Math1 for
739 secretory cell lineage commitment in the mouse intestine. Science 294, 2155–2158.
740 doi:10.1126/science.1065718
741 Yin, X., Farin, H.F., van Es, J.H., Clevers, H., Langer, R., Karp, J.M., 2013. Niche-
742 independent high-purity cultures of Lgr5(+) intestinal stem cells and their progeny. Nat.
743 Methods 11, 106–112. doi:10.1038/nmeth.2737
744 Yu, D.-H., Gadkari, M., Zhou, Q., Yu, S., Gao, N., Guan, Y., Schady, D., Roshan, T.N.,
745 Chen, M.-H., Laritsky, E., Ge, Z., Wang, H., Chen, R., Westwater, C., Bry, L.,
746 Waterland, R.A., Moriarty, C., Hwang, C., Swennes, A.G., Moore, S.R., Shen, L., 2015.
747 Postnatal epigenetic regulation of intestinal stem cells requires DNA methylation and is
748 guided by the microbiome. Genome Biol. 16, 420–16. doi:10.1186/s13059-015-0763-5

749 Yu, S., Tong, K., Zhao, Y., Balasubramanian, I., Yap, G.S., Ferraris, R.P., Bonder, E.M.,
750 Verzi, M.P., Gao, N., 2018. Paneth Cell Multipotency Induced by Notch Activation
751 following Injury. Cell Stem Cell 23, 46–59.e5. doi:10.1016/j.stem.2018.05.002
752 Yui, S., Azzolin, L., Maimets, M., Maimets, M., Pedersen, M.T., Pedersen, M.T., Fordham,
753 R.P., Hansen, S.L., Hansen, S.L., Larsen, H.L., Larsen, H.L., Guiu, J., Guiu, J., Alves,
754 M.R.P., Alves, M.R.P., Rundsten, C.F., Rundsten, C.F., Johansen, J.V., Johansen, J.V.,
755 Li, Y., Li, Y., Madsen, C.D., Madsen, C.D., Nakamura, T., Watanabe, M., Nielsen, O.H.,
756 Schweiger, P.J., Piccolo, S., Jensen, K.B., 2018. YAP/TAZ-Dependent Reprogramming
757 of Colonic Epithelium Links ECM Remodeling to Tissue Regeneration. Cell Stem Cell
758 22, 35–49.e7. doi:10.1016/j.stem.2017.11.001
759 Zhou, A., Lin, K., Zhang, S., Chen, Y., Zhang, N., Xue, J., Wang, Z., Aldape, K.D., Xie, K.,
760 Woodgett, J.R., Huang, S., 2016. Nuclear GSK3β promotes tumorigenesis by
761 phosphorylating KDM1A and inducing its deubiquitylation by USP22. Nat Cell Biol 18,
762 954–966. doi:10.1038/ncb3396
763

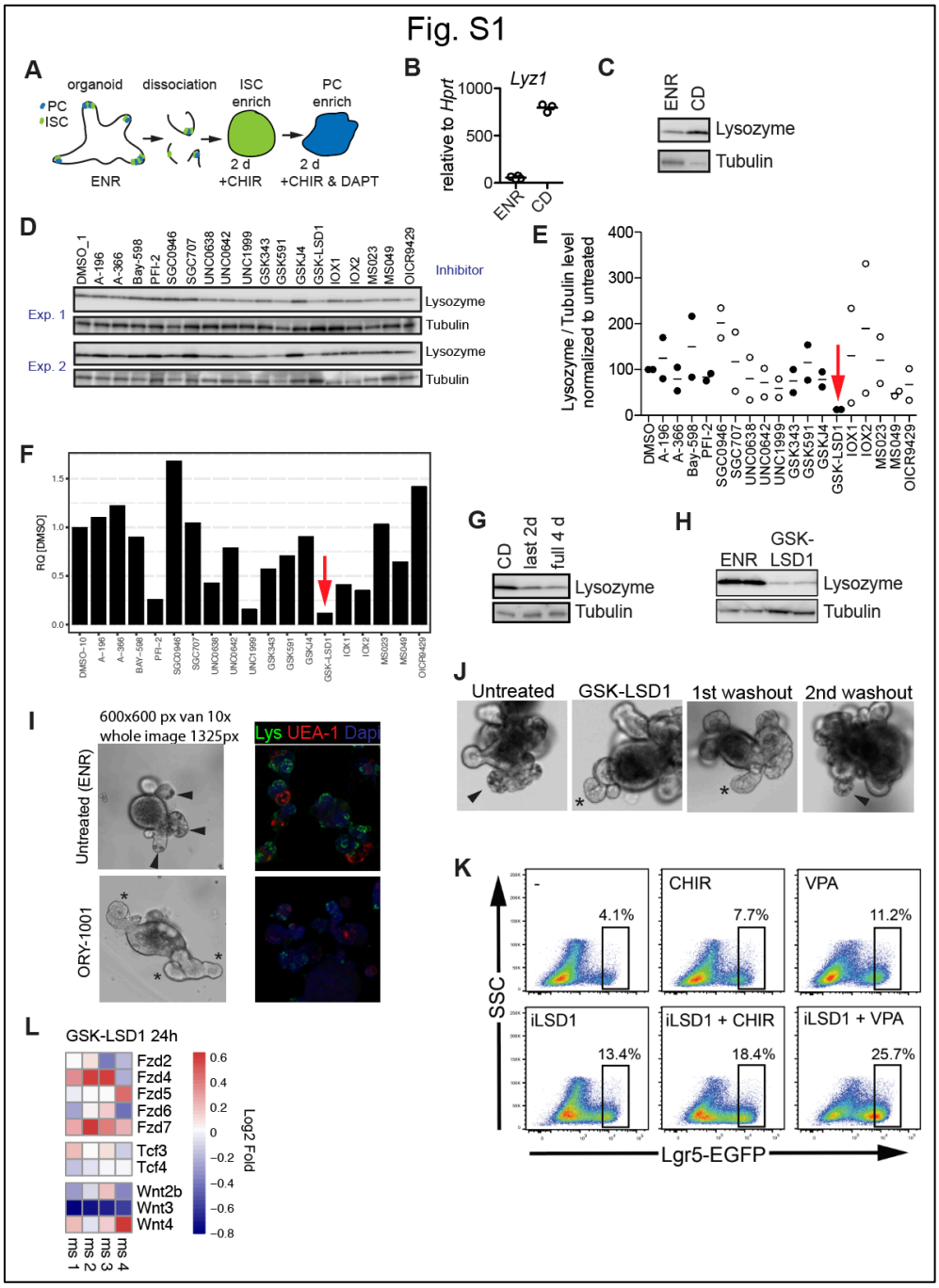

Fig. S1, related to Fig. 1 | A, Schematic overview of organoid PC differentiation protocol. ENR (EGF, Noggin, R-spondin 1).**B,** *Lyz1* expression relative to housekeeping *Hprt* of ENR *vs.* CD cultured organoids. **C&D,** Western blot probed for anti-Lysozyme and anti-Tubulin antibodies of organoid lysates from ENR *vs.* CD cultured organoids (**C**) and CD treated organoids treated with indicated inhibitors. **E,** Quantification of Lysozyme/Tubulin levels by western blot of two independent screens. **F,** A third screen was used to isolate RNA and do *Lyz1* gene expression relative to *Hprt*. GSK-LSD1 was selected as the only probe to impair PC differentiation in all 3 independent experiments (red arrows). **G&H,** Western blot of organoids cultured using the CD protocol (see Fig. S1A), GSK-LSD1 was added at day 0 (full 4d) or day 2 (last 2d). **I,** Organoids were treated with the LSD1 inhibitor ORY-1001 (100 nM) for 4 days. Brightfield images and confocal staining of Lysozyme (Lys in green), UEA-1 (red) and Dapi (blue) is shown. **J,** Representative images of a washout experiment. We observed the return of PCs after the 2nd washout. Arrow depict granular PCs, asterisk depict crypts devoid of organoids. **K,** Flow cytometry of Lgr5-EGFP organoids with indicated treatments. Representative plot of 3 independent experiments. **L,** Heatmap of Wnt related genes of RNA-seq data – PC-specific *Wnt3* is notably downregulated.

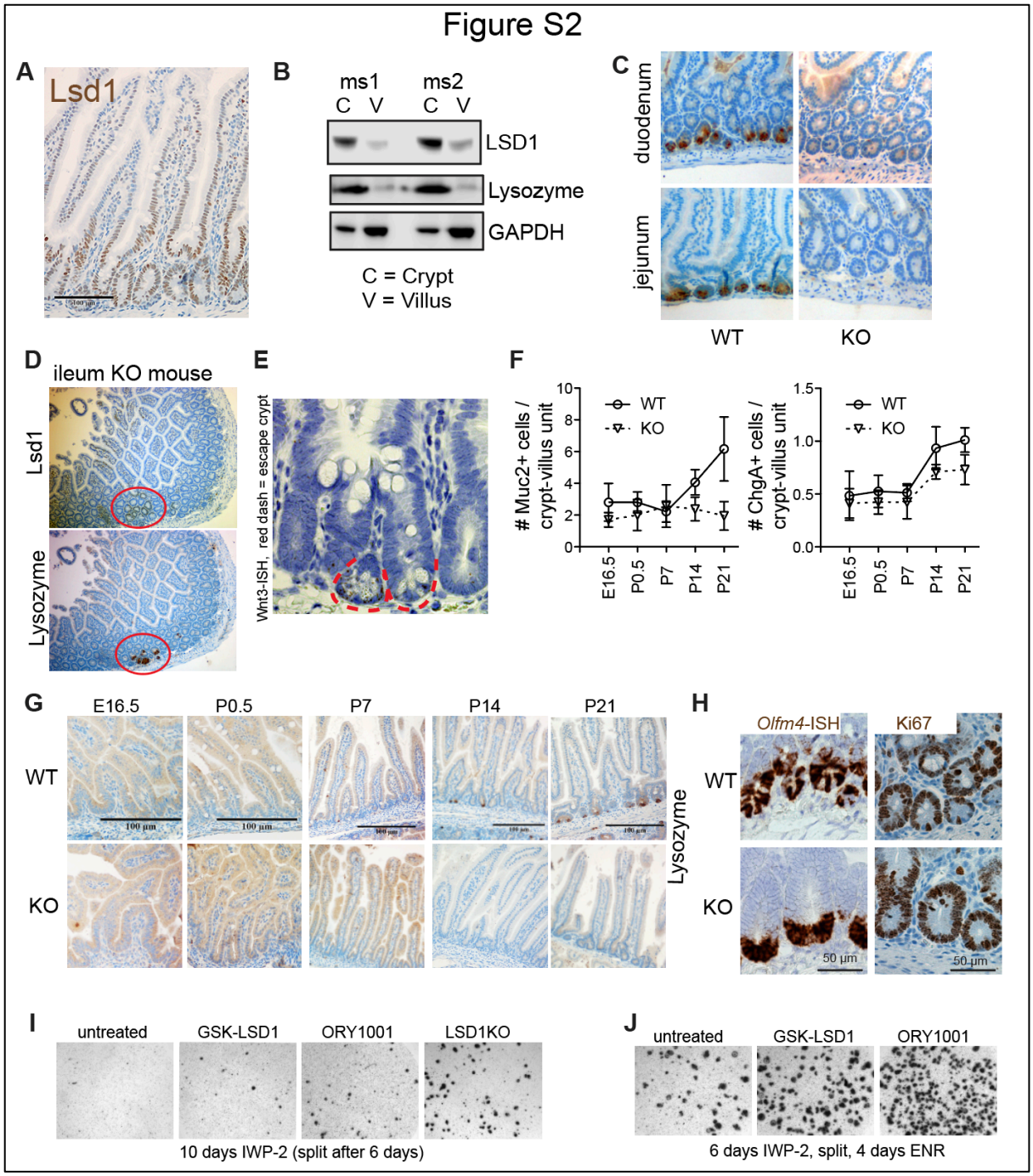

Fig. S2 related to Fig. 2. A, LSD1 antibody staining of adult duodenum tissue. **B,** Western blot probed for indicated proteins isolated from crypt (C) and villus (V) regions from 2 mice. **C,** Images of indicated WT and KO tissue stained for PC marker Lysozyme. **D,** Images of sequential sections of KO small intestine tissue showing that LSD1$^+$ escaper crypts are Lysozyme$^+$. **E,** Image of KO tissue stained for *Wnt3* by *in situ* hybridization. Red-dashed lines indicate escaper crypts containing PCs that express *Wnt3*. **F,** Quantifications of Muc2$^+$ goblet cells and ChgA$^+$ enteroendocrine cells throughout development. N ≥ 3 mice, mean ± SEM is shown. **G,** Images of Lysozyme antibody staining of WT and KO mice throughout development. **H,** Images of *Olfm4*-ISH and Ki67 antibody stained sections of duodenum tissue from adult WT and KO mice. **I & J,** Representative images of organoid cultures treated with indicated inhibitors (GSK-LSD1 5 µM, ORY1001 100 nM, IWP-2 2µM).

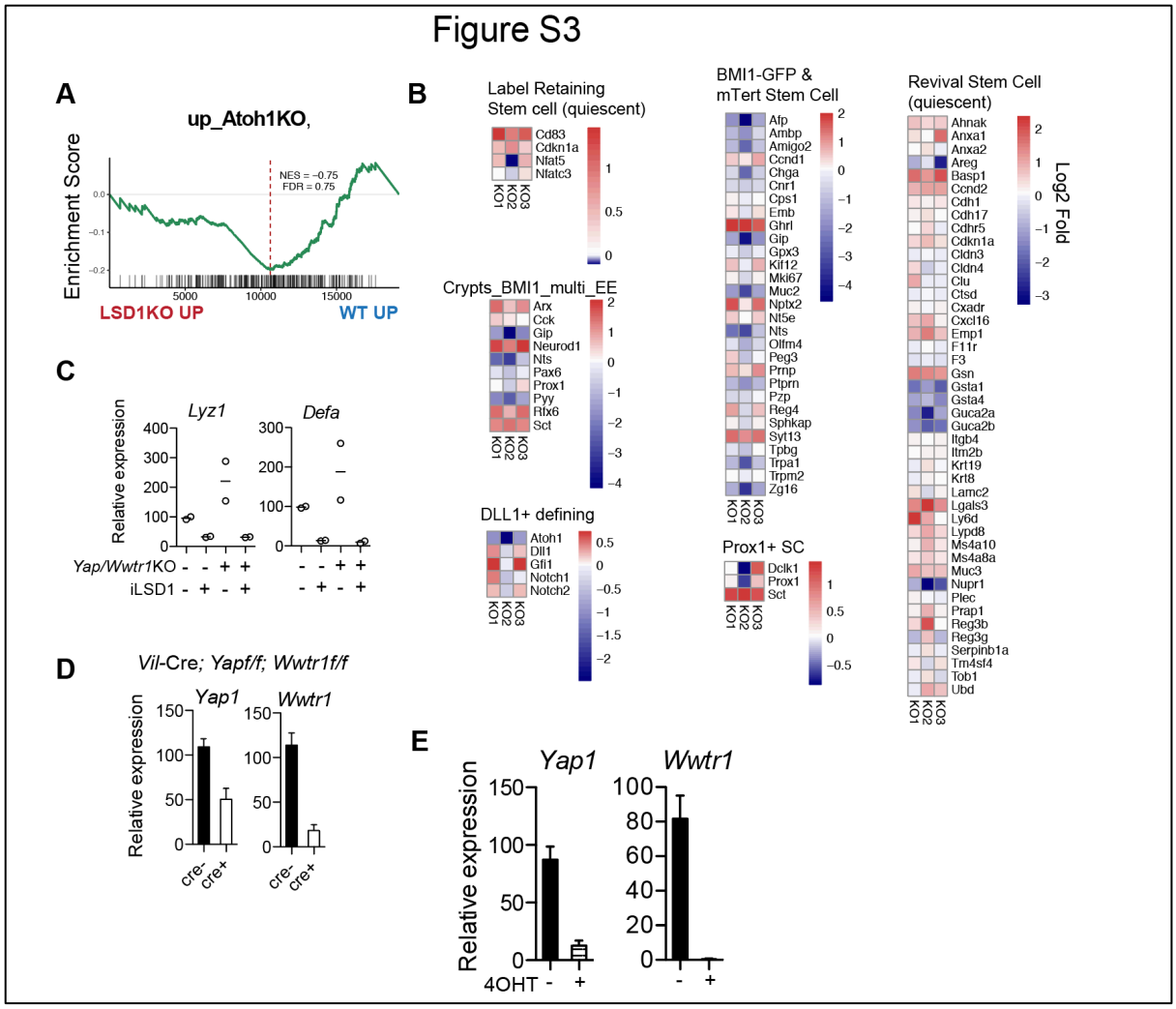

Fig. S3 related to Fig. 3 | A, LSD1KO *vs.* WT RNA-seq data was analyzed by gene set enrichment analysis (GSEA) for indicated gene signature. Normalized Enrichment Score (NES) and False Discovery Rates (FDR) are indicated. **B,** Heatmaps for genes that are associated with or define different types of intestinal stem cells. **C,** qPCR of PC markers *Lyz1* and *Defa* relative to *Gapdh* of organoids from control (Cre-) or mutant (Cre+) *Vil*-Cre; *Yap1*$^{f/f}$; *Wwtr1*$^{f/f}$ mice treated with GSK-LSD1 (as indicated). Means from a representative experiment (n=2) is displayed, performed three times. **D,** Expression of indicated genes by qPCR relative to *Gapdh* from WT (Cre-) and KO (Cre+) organoids derived from *Vil*-Cre; *Yap1*$^{f/f}$; *Wwtr1*$^{f/f}$ mice. Mean + SEM from n=2. **E,** qPCR relative to *Actb* from *Vil*-CreERT2; *Yap1*$^{f/f}$; *Wwtr1*$^{f/f}$ treated with vehicle or 4OH-Tamoxifen (OHT) with or without GSK-LSD1, n=4.

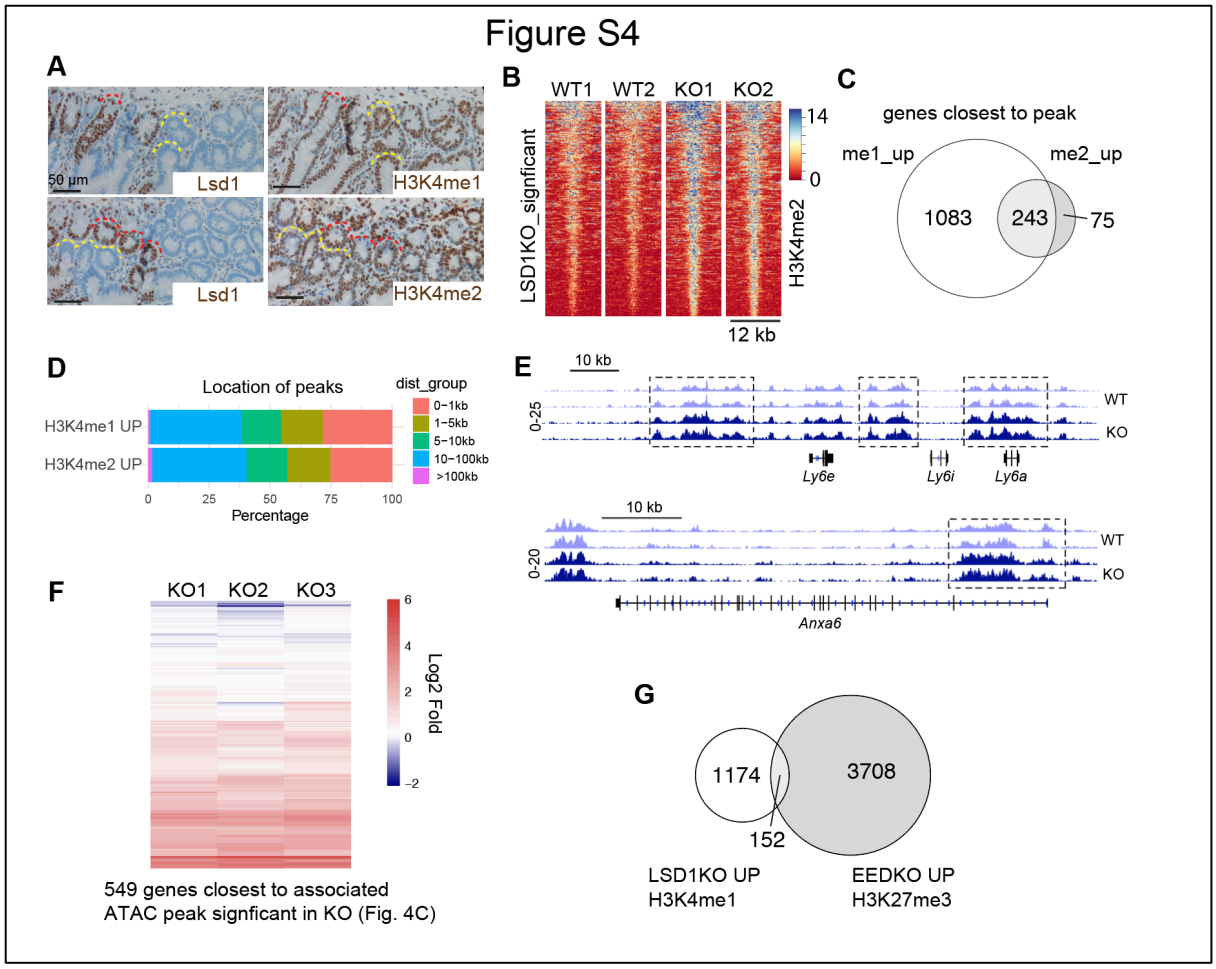

Fig. S4 related to Fig. 4 | A, Images of immune-histochemistry of KO mice including escaper crypts. Yellow=KO crypts, Red=Escaper Lsd1^{+} crypts. **B&C,** Heatmap of H3k4me2 peaks that are significantly up in KO crypts compared to WT crypts. **C,** Venn diagram comparing genes associated with H3K4me1 and H3K4me2 peaks that were significantly higher in KO crypts compared to WT crypts. **D,** Overview of localization relative to TSS of peaks that were up in KO crypts compared to WT crypts for indicated epitopes. **E,** H3K4me1 profiles of indicated loci in WT or KO crypts. Dotted box indicate identification of significant differential peak in the KO. **F,** Heatmap of RNA-seq of genes selected based on upregulated ATAC levels in KO crypts (Fig. 4B). **G,** Venn diagram of genes associated with LSD1 mediated H3K4me1 levels, and genes associated with H3K27me3 peaks.

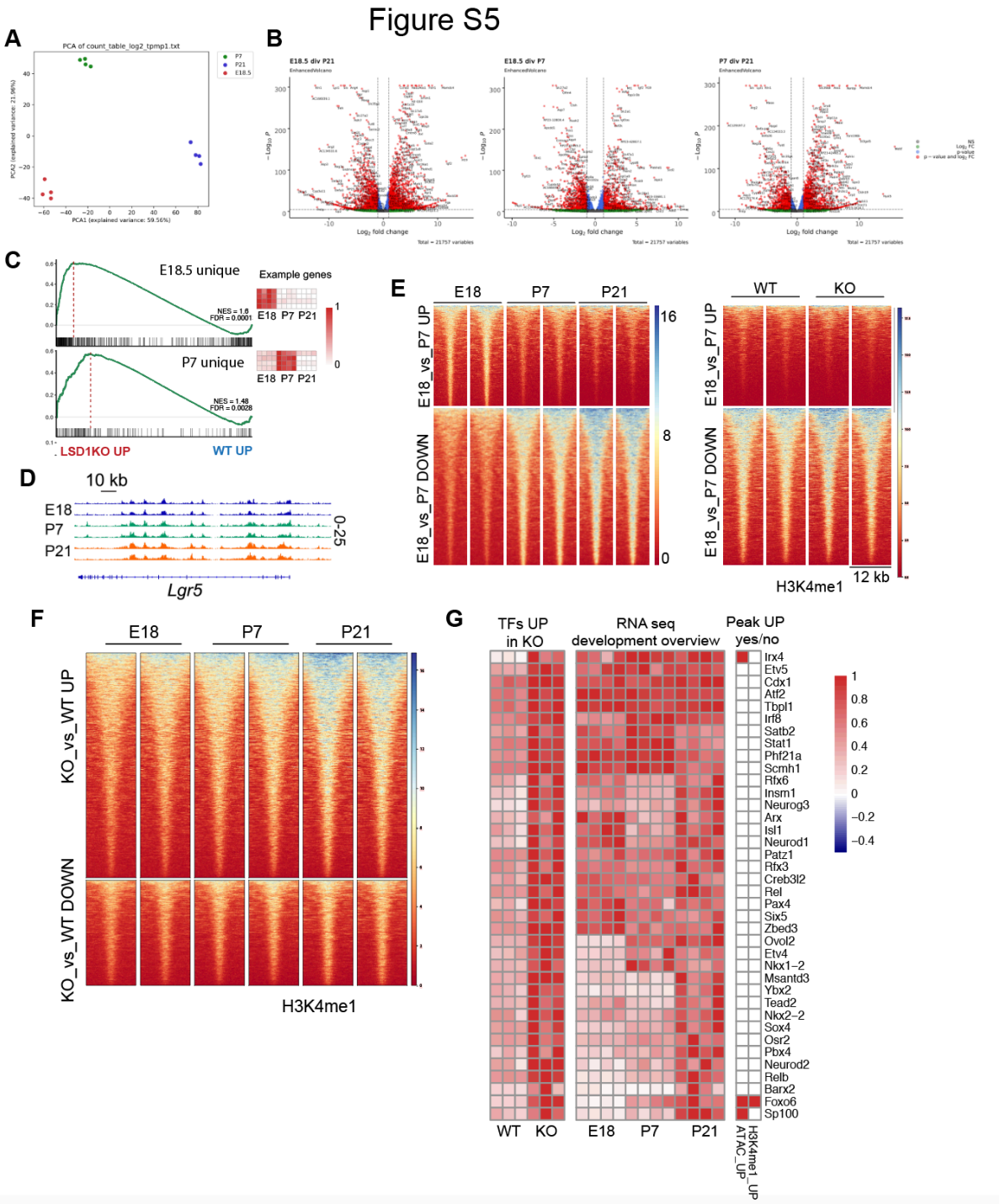

Fig. S5 related to Fig. 5 | A, PCA plot of RNA-seq experiment comparing E18, P7, and P21 intestinal epithelium. **B,** Volcano plots of the differential expression comparing E18, P7, and P21. **C,** GSEA of KO *vs.* WT transcriptional profile on genes that are selectively expressed at E18 or P7 (see heatmaps for examples of gene profiles). **D,** H3K4me1 profiles of *Lgr5* locus at indicated developmental stages. **E,** Heatmap of H3K4me1 sites significantly different between E18 and P7. Left is profile in development, right is profile from WT and KO crypts. **F,** Significant H3K4me1 sites between KO and WT crypts were selected and E18, P7, and P21 H3K4me1 data is displayed. **G,** Heatmaps of transcriptional regulators selected based on upregulation in KO crypts compared to WT crypts. Here are displayed the genes that have no enrichment or enrichment at P21. On the right is displayed whether there are gene-associated increased ATAC or H3K4me1 ChIP levels in KO crypts.

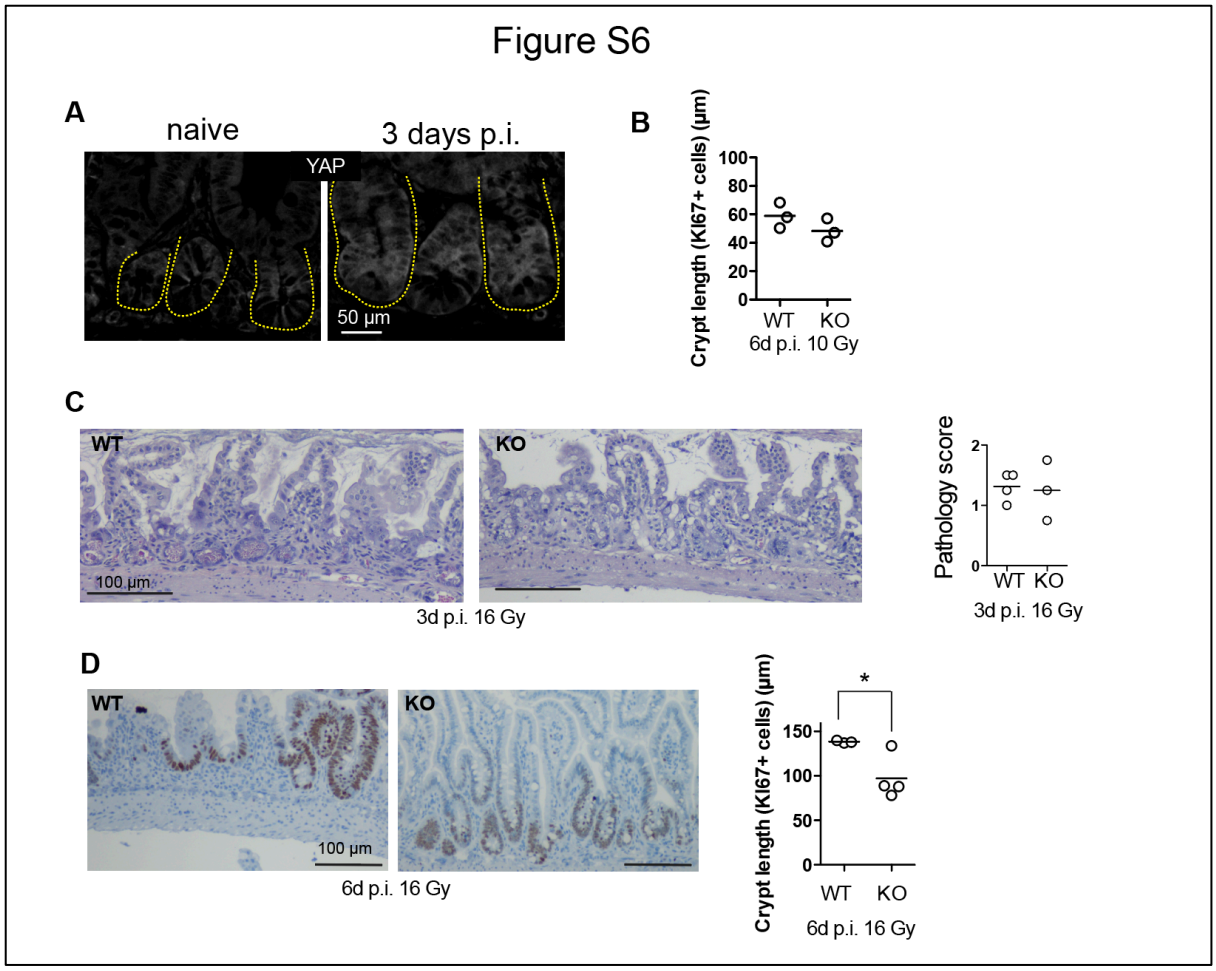

Fig. S6 related to Fig. 6. A, YAP antibody staining of small intestinal crypts (yellow dotted lines) of untreated naive mice, and irradiated (10 gy) mice 3 days post irradiation (p.i.). **B,** Crypt length at 6 days p.i. with 10 Gy. **C,** H&E staining and pathology score of intestines 3 days p.i. with 16 Gy. **D,** Ki67 staining and quantification of Ki67+ crypts at 6 days p.i. with 16 Gy.

METHODS

Animal work

Lgr5-EGFP-IRES-CreERT2 (stock no: 008875) mouse strain was obtained from Jackson Laboratories. *Villin-Cre* and *Villin-CreERT2* (Marjou et al., 2004) were a kind gift from Sylvie Robine, *Lsd1*$^{f/f}$ mice were a kind gift from Dr. Stuart Orkin (Kerenyi et al., 2013). Mice were housed and maintained at the Comparative Medicine Core Facility (CoMed), and experiments were ethically approved by the Norwegian Food Safety Authority (FOTS ID: 11842). Mice were lethally irradiated (10 Gy or 16 Gy) and small intestinal repair was assessed 3 and 6 days post irradiation. *Yap*$^{f/f}$;*Wwtr1*$^{f/f}$ animals (Azzolin et al., 2014) were a kind gift from Stefano Piccolo and were crossed with *Villin-Cre* and *Villin-CreERT2* at University of Copenhagen under the approval of the National Animal Ethics Committee in Denmark.

Crypt, IEC, and ISC isolation, mouse organoid cultures

Adult crypt isolation: Crypt, IEC, and ISC isolation, as well as organoid culture, were essentially done as described (Sato and Clevers, 2013). For adult crypt isolation duodenum tissue was rinsed with ice-cold PBS, cut open longitudinally, and villi were scraped off. Tissue was cut in ~2 mm pieces and washed 5 times with ice-cold PBS. Tissue pieces were incubated in 2 mM EDTA in ice-cold PBS for 30-60 minutes. Crypts were isolated from up to 10 fractions after pipetting up and down 5 times with PBS. To isolate single cells for sorting, crypts were incubated in TrypLE (ThermoFisher) at 37 °C for 20-45 minutes. Single cells were stained and sorted, DAPI-negative and Epcam-positive cells were used for RNA-seq and ChIP-seq experiments. ISCs for clonal organoid outgrowth experiments were isolated by sorting DAPI-negative, GFP-high (top 5%) cells from *Lgr5*-EGFP mice.
E18.5/P7/P21 IEC isolation: Whole (E18.5) or proximal 10 cm (P7 and P21) small intestines were isolated and flushed with ice cold PBS when possible (P21). Small intestines were opened longitudinally (P21 and P7) and cut into small pieces that were washed with ice-cold PBS, and incubated with 2 mM EDTA in ice-cold PBS for 30 min. Whole epithelium was isolated by collecting all fractions, which was used directly for RNA isolation, for ChIP fractions were made single cell using TrypLE (ThermoFisher) and sorted as described.
Organoid cultures: Organoids were grown and maintained in 'basal crypt medium' (Advanced DMEM/F12 medium supplemented with penicillin/streptomycin, 10 mM HEPES, 2 mM Glutamax, N2 (Thermo Fisher, 17502048), B-27 (Thermo Fisher, 17504044)) supplemented with N-acetyl-L-cysteine (Sigma, A7250), 50 ng/ml murine EGF

[ThermoFisher, PMG8041], 20% R-spondin 1s conditioned medium (CM) (kind gift from Dr. Calvin Kuo), and 10% Noggin-CM (kind gift from Dr. Hans Clevers). For ISC clonal experiments, in the first 48 h after seeding, the medium was supplemented with Rock inhibitor (Y-27632) and Jagged-1 peptide (amino-acid sequence *CDDYYYGFGCNKFCRPR,* made in house, peptide synthesized as described (Bolscher et al., 2011)), 33% Wnt3-CM (kind gift from Dr. Hans Clevers) served as control. Medium was renewed every other day. For passaging, organoids cultures were washed, and matrigel and organoids were disrupted mechanically by strong pipetting, centrifuged at 200g, 5 min at 4 °C and resuspended in Matrigel to re-plate. Imaging of live organoids was done using an EVOS FL Auto 2. Structural Genomics Consortium supplied the inhibitors for the screen (www.thesgc.org), all of which are commercially available, concentrations are listed in Supplementary Table 1. Additionally, CHIR99021 (3 µM), IWP-2 (2 µM), VPA (1 mM) and DAPT (10 µM) were used.

Vil-Cre; *Yap*$^{f/f}$/*Wwtr1*$^{f/f}$ and *Vil*-CreERT2; *Yap*$^{f/f}$;*Wwtr1*$^{f/f}$ organoids were cultured in Basal Medium supplemented with NAC, B27, 50ng/ml human EGF (Peprotech, AF-100-15) and 100 ng/ml murine Noggin (Peprotech, 250-38) and either 500 ng/ml mouse RSPO1 (R&D systems, 3474-RS) or 10% RSPO1-conditioned medium. Established *Vil*-CreERT2; *Yap*$^{f/f}$;*Wwtr1*$^{f/f}$ organoids were cultured in the presence of 1 uM 4-OH-Tamoxifen (Sigma-Aldrich) for 72h prior to plating in the absence or presence of GSK-LSD1.

Human organoids. Culture and staining.

Human small intestine samples were obtained from patients undergoing elective surgery at Tokyo University Hospital with written informed consent. This was approved by the ethical committee (No. G3553-(7)). Crypt isolation and optimized organoid culture conditions that allow PC differentiation was done essentially as described[5,6]. In short, stroma was physically removed and the remaining epithelium was cut into 1-mm^3 pieces, washed at least 5 times in ice cold PBS, and incubated in 2.5 mM EDTA in ice cold PBS for 1 hour. Isolated crypts were then suspended in Matrigel and seeded in 48-well plates. Domes of polymerized Matrigel were given the refined medium consisting of 'basal crypt medium' (see above) supplemented with 10 nM gastrin I (Sigma-Aldrich), 1 mM N-acetylcysteine (Sigma-Aldrich), 100 ng/ml recombinant mouse Noggin (PeproTech), 50 ng/ml recombinant mouse EGF (Thermo Fisher Scientific), 100 ng/ml recombinant human IGF-1 (BioLegend), 50 ng/ml recombinant human FGF-basic (FGF-2) (Peprotech), 1 mg/ml recombinant human R-

spondin1 (R&D), 500 nM A83-01 (Tocris) and 50% Afamin-Wnt-3A serum-free conditioned medium. LGR5-iCaspase9-tdTomato organoids were made previously(Fujii et al., 2018). For staining, organoids were isolated from Matrigel using Cell Recovery Solution (Corning) and fixed in 4% paraformaldehyde for 20 min at room temperature. Next, organoids were washed with PBS, and permeabilized with 0.2% Triton X-100 in PBS for 20 min at room temperature. Blocking was done using Power Block Universal Blocking Reagent (BioGenex) for 20 min at room temperature, and rabbit anti-Lysozyme antibody (A0099, DAKO 1:1000 (Fig. 1h), GTX72913, GeneTex, 1:200 (Fig. 2f)) and anti-RFP (600-401-379, Rockland 1:500) was incubated overnight at 4 °C. Organoids were washed 3 times with PBS, and secondary antibody incubation was done for 30 min at room temperature. Nuclear counterstaining was done simultaneously with secondary antibody incubation using Hoechst 33342 (Thermo Fisher Scientific). Stained organoids were suspended in 1 drop of ProLong Diamond Antifade Mountant (Thermo Fisher Scientific) and mounted onto a 35-mm glass bottom dish. Images were captured using a confocal microscope (SP8, Leica).

Immunohistochemical staining of intestinal tissue

For immunohistochemical staining and imaging, tissues were harvested and fixed in swiss rolls. After fixation in formalin, tissues were embedded in paraffin and cut in 4 µm sections. Paraffin sections were rehydrated and peroxidase activity was blocked in 3% hydrogen peroxide. Antigen retrieval was performed in citrate buffer pH6. Sections were stained overnight with primary antibodies against Ki67 (1:500, Thermo Scientific MA5-14520), Lysozyme (1:750, Dako A0099), Sox9 (1:200, Millipore), LSD1 (1:200, Cell Signalling 2184S), H3K4me1 (1:100, Cell Signaling 9723) and H3K4me2 (1:1500, Cell Signalling 9725). The sections were washed in TBS and Tween-20 and stained for 1 hour with HRP-labelled secondary antibody (Dako K4003). The staining was developed with diaminobenzidine (DAB) chromogenic substrate (Dako K5007) and mounted with Glycergel mounting medium (Dako C056330). Tissues were imaged using a Nikon eclips Ci-L microscope.

Immunofluorescence staining of intestinal tissue and organoids

For immunofluorescence labeling and imaging, tissues (first 5 cm of duodenum) were harvested and fixed in swiss rolls. After fixation in formalin, tissues were paraffin embedded and cut in 4 µm sections. Briefly, paraffin sections were treated as before for IHC, and after antigen retrieval were blocked and permeabilized in PBS with TX-100 0.2%, Normal Goat

Serum (NGS) 2%, BSA 1% and Tween-20 0.05%. Sections were then stained overnight in the same blocking buffer with primary antibodies against GFP (1:2000 Abcam 13970), YAP (1:200 Cell Signaling Technologies 14074S), OLFM4 (1:200 Cell Signalling 39141S) or LSD1 (1:200 Cell Signaling Technologies 2184S). Tissues were then incubated with the corresponding secondary antibodies for 3 hours (1:500 Alexa Fluor), Rhodamine-labeled UEA1 (5 µg/ml Thermo Fisher Scientific NC9290135) and Hoechst 33342 (1:10,000). Washes were performed with PBS + Tween-20 0.1%.

For organoid staining, organoids were grown in Matrigel on eight-chamber µ-slides (Ibidi 80826) and fixed after exposition to the specific treatments in PBS containing 4% paraformaldehyde (pH 7.4) and 2% sucrose for 20-30 min, permeabilized (PBS, 0.2% Triton X-100) and blocked (PBS-Triton X-100 0.2%, 2% NGS, 1% BSA). Primary antibodies against the following antigens were used, diluted in the same blocking buffer: Lysozyme (1:500, Dako A0099), GFP (1:2000 Abcam 13970) and LSD1 (1:400 Cell Signaling Technologies 2184S) overnight at 4°C with slow agitation. Rhodamine-labeled UEA1 (5 µg/ml Thermo Fisher Scientific NC9290135) and Hoechst 33342 (1:10,000) were used to stain secretory cells and nuclei respectively together with the corresponding secondary antibodies (1:500 Alexa Fluor) and incubated overnight in PBS with 0.2% Triton X-100, 1% NGS and 0.5% BSA at 4°C. Tissue sections and organoids were both mounted using Fluoromount G (ThermoFisher Scientific, 00-4958-02) and imaged with a Zeiss 510 Meta Live or a Zeiss LSM880 confocal microscope, using 20x and 40x objective lens.

In situ hybridization

In situ hybridization was performed on FFPE tissues using RNAscope® 2.5 HD BROWN reagent kit (Advanced Cell Diagnostics (ACD) 322371). Tissue sections (4µm) were deparaffinised with Neoclear and 100% ethanol. The slides were pretreated with hydrogen peroxide for 10 minutes, target antigen retrieval reagent for 15 minutes, and protease plus reagent for 30 minutes (ACD 322300 and 322000). The sections were hybridized with probes for Mm-Wnt3 (ACD 312241), Mm-Olfm4 (ACD 311831), Mm-Atoh1 (ACD 408791), positive control Mm-Ppib (ACD 313911) and negative control Mm-DapB (ACD 310043). For amplification and chromogenic detection the 2.5 HD Detection Reagents BROWN kit (ACD 322310) was used. The slides were counterstained with hematoxylin, dehydrated and mounted with Neomount (Merck 109016). Tissues were imaged using a Nikon eclips Ci-L microscope.

Flow cytometry analysis of organoids

Organoids were mechanically disrupted, centrifuged at 2000 rpm and incubated with TripLE (ThermoFisher) at 37 degrees Celsius for 50 minutes for dissociation into single cells. Cells were incubated with DAPI and analyzed using a flow cytometer (FACSCanto II; BD). Stem cell populations were gated as DAPI negative and GFP-high (top 5%) and analyzed using FlowJo software.

Western Blot

Organoids were harvested in lysis buffer (1% NP-40, 0.02% SDS in 1X TBS) on ice for 30 minutes. Debris was pelleted by spinning down at 14 000 RPM for 30 min. Supernatant was diluted in 4x NuPage sample buffer with 100 mM DTT, and samples were run using precast 4-12% gels using the NuPage system, and blotted using iblot 2 (all ThermoFisher). Membranes were incubated with antibodies against Lysozyme (Dako A0099), Tubulin (Abcam Ab6046), Yap/Taz (Santa Cruz, SC-101199). Secondary antibodies (HRP linked) were swine anti–rabbit (P039901-2) and goat anti–mouse (P044701-2) (DAKO). Imaging was done using SuperSignal West Femto (ThermoFisher) on a Lycor machine. Bands were quantified using Image Studio software.

qPCR

RNA from organoids was isolated using either an RNeasy kit (Qiagen) or Quick-RNA kit (Zymo). Reverse transcription was carried out by using the High-Capacity RNA-to-cDNA Kit (ThermoFisher). Quantitive PCR was performed using the QuantiFast SYBR Green PCR Kit (Qiagen) using primers for *Hprt* (fwd: cctcctcagaccgcttttt, rev: aacctggttcatcatcgctaa), *Actb* (fwd: actaatggcaacgagcggttc, rev: ggatgccagaggattccatacc), *Lyz1* (fwd: ggcaaaaccccaagatctaa, rev: tctctcaccaccctctttgc), *Lyz1* (fwd: gccaaggtctacaatcgttgtgagttg, rev: cagtcagccagcttgacaccacg), Defa, fwd: aatcctcctctctgccctcg, rev: accagatctctcaatgattcctct), *Yap1* (fwd: tggccaagacatcttctggt, rev: caggaacgttcagttgcgaa), *Wwtr1* (fwd: tggggttagggtgctacagt, rev: ggattgacggtcatgggtgt), *Gapdh* (fwd: tgttcctacccccaatgtgt, rev: tgtgagggagatgctcagtg), *Olfm4* (fwd: ggatcctgaacttttggtgct, rev: acgccaccatgactacagc), and *Wnt3* (fwd: ctcgctggctacccaattt, rev: gaggccagagatgtgtactgc). Samples were commonly analyzed in duplicate and RNA expression was calculated either normalized to reference gene, or additionally normalized to control conditions.

RNAseq preparation

RNA for WT and LSD1KO crypts was isolated by sorting IECs (DAPI-, Epcam+) in 2x RNA shield buffer (Zymo) and RNA isolation using the Quick-RNA Micro prep kit (Zymo). Library preparation was done using the Illumina TruSeq Stranded protocol, and samples were sequenced at 75X2 bp PE reads on an Illumina NS500 MO flow-cell. Sequencing was performed by the Genomics core facility (GCF, NTNU). Crypts from E18.5, P7 and E18.5 was directly dissolved in RNA isolation buffer and RNA was isolated using the Quick-RNA micro prep kit (Zymo). Library preparation was done using the NEB Next® Ultra™ RNA Library Prep Kit. Sequencing was performed by Novogene (UK) Co.

RNAseq analysis

Sequenced reads were aligned with STAR to the *Mus musculus* genome build mm10 (Dobin et al., 2013; Frankish et al., 2019). The number of reads that uniquely aligned to the exon region of each gene in GENCODE annotation M18 of the mouse genome was then counted using featureCounts (Liao et al., 2014). Genes that had a total count less than 10 were filtered out. Differential expression was then determined with DESeq2 using default settings (Love et al., 2014). Interesting differential genes were plotted with a volcano plot using the R package EnhancedVolcano. Heatmaps where generated using the R-package pheatmap. Count values for each gene were transformed to rates per bp by dividing the count for a gene by the length of the total exon region for that gene. Rates per bp where then converted to Transcripts Per Million (TPM) by dividing the rate per bp for each gene by the sum of rates per bp for all the genes in that sample and multiplying with one million. PCA analysis was performed using the function sklearn.decomposition.PCA in scikit-learn. Gene set enrichment analysis (GSEA) was done by sorting the output from DESeq2 by log2 fold change and with the log2 fold change as weights. GSEA was run with the R package clusterProfiler using 10000 permutations and otherwise default settings. Gene sets were generated from published datasets and can be found in supplementary table 3.

Microarray analysis

Gene expression in human small intestinal organoids was analyzed using the PrimeView Human Gene Expression Array. Raw expression data were normalized with the rma function in the R/Bioconductor package affy and the normalized values were used to calculate log fold change(Gautier et al., 2004). For each gene, the probe with the highest absolute log fold change was used. GSEA was run on this list of genes as described for the RNAseq analysis.

ChIP-seq

DAPI-negative, Epcam-positive IECs were sorted in PBS containing 20 mM Sodium Butyrate, and cross-linked by incubation in 1% formaldehyde for 8 minutes. Glycine was added to a final concentration of 125 mM and incubated for 5 minutes at room temperature. Using a swing-out rotor cells were washed 3 times in ice-cold PBS with 20 mM Sodium Butyrate. After washing, cells were snap frozen in liquid nitrogen and stored in -80 °C. The ChIP-seq was carried out similarly to previously described protocols(Dahl and Collas, 2008)

Binding of antibodies to paramagnetic beads. The stock of paramagnetic Dynabeads Protein A was vortexed thoroughly to ensure a homogenous suspension before pipetting. Dynabeads stock solution (5 µL per IP) was transferred into a 1.5-ml tube, which was placed on a magnetic rack and the beads captured on the tube wall. The buffer was discarded, the beads washed twice with 200 µL standard RIPA buffer (10 mM Tris-HCl pH 8.0, 140 mM NaCl, 1 mM EDTA, 0.5 mM EGTA, 1% Triton X-100, 0.1% SDS, 0.1% Na-deoxycholate) and resuspended in standard RIPA buffer to a final volume of 100 uL per IP. 99 µL of this was aliquoted into each 0.6 mL tube on ice, and antibody (1.2 ug of anti-H3K4me1: Diagenode, C15410194, Lot A1862D or 4 uL anti-H3K4me2: Cell Signaling #9725, Lot 9) was added per 0.6 mL-tube. Tubes were then incubated at 40 r.p.m. on a 'head-over-tail' tube rotator for at least 16h at 4 °C.

Chromatin preparation, Lsd1 cre+ / cre-. Crosslinked cell pellets containing 335 000-500 000 cells were thawed on ice. The 6-10µL pellets were added Lysis buffer (50 mM Tris–HCl pH 8.0, 10 mM EDTA pH 8.0, 1% SDS, 20 mM sodium butyrate, 1 mM PMSF and protease inhibitor cocktail) to a total of 160 µL and incubated on ice for 10 min. The samples were sonicated for 8 x 30 s using a UP100H Ultrasonic Processor (Hielscher) fitted with a 2-mm probe. We allowed for 30 s pauses on ice between each 30 s session, using pulse settings with 0.5 s cycles and 27% power. After the final sonication, 340 µL standard RIPA (with 20 mM sodium butyrate, 1 mM PMSF and protease inhibitor cocktail) was added to the tube while washing the probe, followed by thorough mixing by pipetting. 20 µL was removed as input, and the remaining solution was diluted further with 1mL standard RIPA buffer (with 20 mM sodium butyrate, 1 mM PMSF and protease inhibitor cocktail). The samples and inputs were centrifuged at 12,000 g in a swinging-bucket rotor for 10 min at 4 °C and the supernatants were transferred to a 1.5-ml tube on ice. 66 000 – 100 000 cells were used per IP.

Chromatin preparation, E18.5/P7/P21. The H3K4me1 ChIP-seq for the different developmental stages was slightly modified at the chromatin preparation step. Crosslinked cell pellets containing 50 000-300 000 cells were thawed on ice. The 10 µL pellets were added a modified Lysis buffer (50 mM Tris–HCl pH 8.0, 10 mM EDTA pH 8.0, 0.8% SDS, 20 mM sodium butyrate, 1 mM PMSF and protease inhibitor cocktail) to a total of 120µL and incubated on ice for 10 min, followed by addition of 30 uL PBS with 20 mM sodium butyrate. The samples were sonicated as described above. After the final sonication, 360 uL RIPA without SDS (with 20 mM sodium butyrate, 1 mM PMSF and protease inhibitor cocktail) was added to the tube while washing the probe, followed by thorough mixing by pipetting. The sample and input were centrifuged at 12,000g in a swinging-bucket rotor for 10 min at 4 °C and the supernatants were transferred to a 1.5 ml-tube on ice. Chromatin corresponding to 1 000 - 2 000 cells was removed from each sample to be decross-linked and sequenced as inputs. For the ChIPs, chromatin corresponding to 50 000 cells was used for E18.5 Replicate A, while chromatin from 100 000 cells was used for the remaining samples
Immunoprecipitation and washes. Pre-incubated antibody–bead complexes were washed twice in 200 µl standard RIPA buffer by vortexing roughly. The tubes were centrifuged in a mini-centrifuge to bring down any solution trapped in the lid and antibody–bead complexes were captured in a magnetic rack. After removal of RIPA, 177-500 µl of chromatin (equivalent of 50,000-100,000 cells per ChIP) was added to each tube, then incubated at 4 °C, 40 r.p.m. on a 'head-over-tail' rotator for at least 16 h. For H3K4me1 ChIPs, the chromatin–antibody–bead complexes were washed three times in 100 µl ice-cold standard RIPA buffer. For H3K4me2 ChIPs, the reactions were washed once in standard RIPA, once in RIPA with increased salt and SDS (300 mM NaCl and 0.20% SDS), once in RIPA with increased salt and SDS (300 mM NaCl and 0.23% SDS), once in standard RIPA. All washing steps were performed with 100uL ice cold buffer supplemented with 20 mM sodium butyrate, 1 mM PMSF and protease inhibitor cocktail. Each wash involved rough vortexing at full speed, repeated twice with pauses on ice in between. Next, a wash in 100µl TE and tube shift was carried out.
DNA isolation and purification. TE was removed and 150µl ChIP elution buffer was added (20 mM Tris-HCl pH 7.5, 50 mM NaCl, 5 mM EDTA. 1% SDS, 30 µg RNase A) and incubated at 37 °C, 1 h at 1,200 r.p.m. on a Thermomixer. The input samples were added ChIP elution buffer up to 150uL and incubated similarly. 1µl of Proteinase K (20 mg/ml stock) was added to each ChIP or input tube and incubated at 68 °C, 4 h at 1,250 r.p.m. The ChIP eluates were transferred to a 1.5-ml tube. Then, a second elution with 150µl was

performed for 5 min and pooled with the first supernatant. The ChIP and input DNA was purified by phenol-chloroform isoamylalcohol extraction, ethanol-precipitated with 11µl acrylamide carrier and dissolved in 10-15µl EB (10 mM Tris-HCl).

Library preparation and sequencing. ChIP and input library preparations were performed according to the QIAseq Ultralow Input Library Kit procedure. Sequencing procedures were carried out according to Illumina protocols, on a NextSeq 500 instrument, with 75bp single end reads using high output reagents. The sequencing service was provided by the Norwegian Sequencing Centre (www.sequencing.uio.no).

ATAC-seq

Cells were harvested and frozen in culture media containing FBS and 10% DMSO. Cryopreserved cells were sent to Active Motif to perform the ATAC-seq assay. The cells were then thawed in a 37ºC water bath, pelleted, washed with cold PBS, and tagmented as previously described (Buenrostro et al., 2013), with some modifications based on (Corces et al., 2017). Briefly, cell pellets were resuspended in lysis buffer, pelleted, and tagmented using the enzyme and buffer provided in the Nextera Library Prep Kit (Illumina). Tagmented DNA was then purified using the MinElute PCR purification kit (Qiagen), amplified with 10 cycles of PCR, and purified using Agencourt AMPure SPRI beads (Beckman Coulter). Resulting material was quantified using the KAPA Library Quantification Kit for Illumina platforms (KAPA Biosystems), and sequenced with PE42 sequencing on the NextSeq 500 sequencer (Illumina).

Analysis of ATAC-seq data was very similar to the analysis of ChIP-Seq data. Reads were aligned using the BWA algorithm (mem mode; default settings). Duplicate reads were removed, only reads mapping as matched pairs and only uniquely mapped reads (mapping quality >= 1) were used for further analysis. Alignments were extended in silico at their 3'-ends to a length of 200 bp and assigned to 32-nt bins along the genome. The resulting histograms (genomic "signal maps") were stored in bigWig files. Peaks were identified using the MACS 2.1.0 algorithm at a cutoff of p-value 1e-7, without control file, and with the –nomodel option. Peaks that were on the ENCODE blacklist of known false ChIP-Seq peaks were removed. Signal maps and peak locations were used as input data to Active Motifs proprietary analysis program, which creates Excel tables containing detailed information on sample comparison, peak metrics, peak locations and gene annotations.

ChIP-seq and ATAC-seq analysis

Sequence reads were deduplicated with BBMaps clumpify tool and then aligned with STAR to the *Mus musculus* genome build mm10 (Dobin et al., 2013; Frankish et al., 2019) (*Bushnell, B. BBMap. SourceForge Available at: https://sourceforge.net/projects/bbmap Accessed: 12th February 2019*). Peaks were identified using Model-Based analysis of ChIP-seq 2 (MACS2) with peak type set to broad and genome size 2652783500 (Zhang et al., 2008). Input files where supplied for H3K4me1/2 but not for ATAC seq. Peaks from all samples that were compared in differential expression were merged with BEDTools to create a union set and featureCounts was used to count the number of reads, including multi-mappers, for each sample in the union set of peaks (Zhang et al., 2008). Differential peaks was determined from the counts with DESeq2 (Love et al., 2014) using default settings and. deepTools2 was used to create heatmaps (Ramírez et al., 2016). Peak locations were associated with the gene that has the closest transcriptional start site (TSS) with the closest command in bedtools (Quinlan and Hall, 2010). Ties were resolved by only reporting the first hit. TSS sites were downloaded from biomart for GRCm38.p6. The peaks were grouped on the distance to the TSS and the size of each group was plotted. The list of differential peaks with associated genes was grouped by gene and sorted on the differential peak that had the smallest p-value for each gene. Each gene was determined to be either up or down in signal based on whether the total change was above or below zero, where total change is defined as the average of log fold change multiplied by peak length of all peaks associated with that gene. Venn diagrams where created with the R package Euler (Larsson2018, n.d.). Bigwig files describing the score across the genome were created with deepTools2 and scaled to the count of the sample with the least aligned reads for each group (e.g. H3K4me1, H3K4me2 and ATAC) (Ramírez et al., 2016). Heatmaps of regions of interest was created with deepTools2. Chipseq profiles were created in integrative genomics viewer (IGV) (Robinson et al., 2011).

Fetal RNAseq (from Yui et al)

Published microarray raw data was downloaded from ArrayExpress under the accession number “E-MTAB-5246”, normalized with “neqc” function in the R package limma and then log2fc was calculated from the normalized expression values (Ritchie et al., 2015; Yui et al., 2018). GSEA was performed as described in the RNAseq methods.

scRNAseq analysis

Preprocessed and normalized scRNAseq data where downloaded from GSE117783 (Ayyaz et al., 2019). The control treated cells where randomly sub sampled so the two groups had equal number of cells and the density of LSD1 expressing cells where plotted in base R. Y-axis is shortened to show distribution of cells that has an expression larger than zero.

Statistical analysis

Statistical significance was determined either using Student's *t* test or 1-way ANOVA with Tukey's post hoc test, or, when n<10 non-parametric testing (Mann Whitney test) was done. Significance levels are indicated in figure legends.

Data availability statement

All raw data is available through ArrayExpress. WT/KO Crypt RNAseq: E-MTAB-7862, WT/KO Crypt ChIP seq: E-MTAB-7871, WT/KO Crypt ATAC: E-MTAB-8718, E18/P7/P21 RNA-seq E-MTAB-8713, E18/P7/P21 H3K4me1 ChIP-seq: E-MTAB-8710 and Human microarray: E-MTAB-7871.

Extended data references

Ayyaz, A., Kumar, S., Sangiorgi, B., Ghoshal, B., Gosio, J., Ouladan, S., Fink, M., Barutcu, S., Trcka, D., Shen, J., Chan, K., Wrana, J.L., Gregorieff, A., 2019. Single-cell transcriptomes of the regenerating intestine reveal a revival stem cell. Nature 569, 121–125. doi:10.1038/s41586-019-1154-y

Azzolin, L., Panciera, T., Soligo, S., Enzo, E., Bicciato, S., Dupont, S., Bresolin, S., Frasson, C., Basso, G., Guzzardo, V., Fassina, A., Cordenonsi, M., Piccolo, S., 2014. YAP/TAZ Incorporation in the β-Catenin Destruction Complex Orchestrates the Wnt Response. Cell 158, 157–170. doi:10.1016/j.cell.2014.06.013

Bolscher, J.G.M., Oudhoff, M.J., Nazmi, K., Antos, J.M., Guimaraes, C.P., Spooner, E., Haney, E.F., Garcia Vallejo, J.J., Vogel, H.J., van't Hof, W., Ploegh, H.L., Veerman, E.C.I., 2011. Sortase A as a tool for high-yield histatin cyclization. Faseb J 25, 2650–2658. doi:10.1096/fj.11-182212

Buenrostro, J.D., Giresi, P.G., Zaba, L.C., Chang, H.Y., Greenleaf, W.J., 2013. Transposition of native chromatin for fast and sensitive epigenomic profiling of open chromatin, DNA-binding proteins and nucleosome position. Nat. Methods 10, 1213–1218. doi:10.1038/nmeth.2688

Corces, M.R., Trevino, A.E., Hamilton, E.G., Greenside, P.G., Sinnott-Armstrong, N.A., Vesuna, S., Satpathy, A.T., Rubin, A.J., Montine, K.S., Wu, B., Kathiria, A., Cho, S.W., Mumbach, M.R., Carter, A.C., Kasowski, M., Orloff, L.A., Risca, V.I., Kundaje, A., Khavari, P.A., Montine, T.J., Greenleaf, W.J., Chang, H.Y., 2017. An improved ATAC-seq protocol reduces background and enables interrogation of frozen tissues. Nat. Methods 14, 959–962. doi:10.1038/nmeth.4396

Dahl, J.A., Collas, P., 2008. A rapid micro chromatin immunoprecipitation assay (ChIP). Nat Protoc 3, 1032–1045. doi:10.1038/nprot.2008.68

Dobin, A., Davis, C.A., Schlesinger, F., Drenkow, J., Zaleski, C., Jha, S., Batut, P., Chaisson, M., Gingeras, T.R., 2013. STAR: ultrafast universal RNA-seq aligner. Bioinformatics 29, 15–21. doi:10.1093/bioinformatics/bts635

Frankish, A., Diekhans, M., Ferreira, A.-M., Johnson, R., Jungreis, I., Loveland, J., Mudge, J.M., Sisu, C., Wright, J., Armstrong, J., Barnes, I., Berry, A., Bignell, A., Carbonell Sala, S., Chrast, J., Cunningham, F., Di Domenico, T., Donaldson, S., Fiddes, I.T., García Girón, C., Gonzalez, J.M., Grego, T., Hardy, M., Hourlier, T., Hunt, T., Izuogu, O.G., Lagarde, J., Martin, F.J., Martínez, L., Mohanan, S., Muir, P., Navarro, F.C.P., Parker, A., Pei, B., Pozo, F., Ruffier, M., Schmitt, B.M., Stapleton, E., Suner, M.-M., Sycheva, I., Uszczynska-Ratajczak, B., Xu, J., Yates, A., Zerbino, D., Zhang, Y., Aken, B., Choudhary, J.S., Gerstein, M., Guigó, R., Hubbard, T.J.P., Kellis, M., Paten, B., Reymond, A., Tress, M.L., Flicek, P., 2019. GENCODE reference annotation for the human and mouse genomes. Nucleic Acids Res. 47, D766–D773. doi:10.1093/nar/gky955

Fujii, M., Matano, M., Toshimitsu, K., Takano, A., Mikami, Y., Nishikori, S., Sugimoto, S., Sato, T., 2018. Human Intestinal Organoids Maintain Self-Renewal Capacity and Cellular Diversity in Niche-Inspired Culture Condition. Cell Stem Cell 23, 787–793.e6. doi:10.1016/j.stem.2018.11.016

Gautier, L., Cope, L., Bolstad, B.M., Irizarry, R.A., 2004. affy--analysis of Affymetrix GeneChip data at the probe level. Bioinformatics 20, 307–315. doi:10.1093/bioinformatics/btg405

Kerenyi, M.A., Shao, Z., Hsu, Y.-J., Guo, G., Luc, S., O'Brien, K., Fujiwara, Y., Peng, C., Nguyen, M., Orkin, S.H., 2013. Histone demethylase Lsd1 represses hematopoietic stem and progenitor cell signatures during blood cell maturation. Elife 2, e00633. doi:10.7554/eLife.00633

Larsson, J., 2018, n.d. eulerr: area-proportional Euler and Venn diagrams with ellipses.

Liao, Y., Smyth, G.K., Shi, W., 2014. featureCounts: an efficient general purpose program for assigning sequence reads to genomic features. Bioinformatics 30, 923–930. doi:10.1093/bioinformatics/btt656

Love, M.I., Huber, W., Anders, S., 2014. Moderated estimation of fold change and dispersion for RNA-seq data with DESeq2. Genome Biol. 15, 550. doi:10.1186/s13059-014-0550-8

Marjou, El, F., Janssen, K.-P., Chang, B.H.-J., Li, M., Hindie, V., Chan, L., Louvard, D., Chambon, P., Metzger, D., Robine, S., 2004. Tissue-specific and inducible Cre-mediated recombination in the gut epithelium. Genesis 39, 186–193. doi:10.1002/gene.20042

Quinlan, A.R., Hall, I.M., 2010. BEDTools: a flexible suite of utilities for comparing genomic features. Bioinformatics 26, 841–842. doi:10.1093/bioinformatics/btq033

Ramírez, F., Ryan, D.P., Grüning, B., Bhardwaj, V., Kilpert, F., Richter, A.S., Heyne, S., Dündar, F., Manke, T., 2016. deepTools2: a next generation web server for deep-sequencing data analysis. Nucleic Acids Res. 44, W160–5. doi:10.1093/nar/gkw257

Ritchie, M.E., Phipson, B., Wu, D., Hu, Y., Law, C.W., Shi, W., Smyth, G.K., 2015. limma powers differential expression analyses for RNA-sequencing and microarray studies. Nucleic Acids Res. 43, e47–e47. doi:10.1093/nar/gkv007

Robinson, J.T., Thorvaldsdottir, H., Winckler, W., Guttman, M., Lander, E.S., Getz, G., Mesirov, J.P., 2011. Integrative genomics viewer. Nature Biotechnology 29, 24–26. doi:10.1038/nbt.1754

Sato, T., Clevers, H., 2013. Primary mouse small intestinal epithelial cell cultures. Methods Mol. Biol. 945, 319–328. doi:10.1007/978-1-62703-125-7_19

Yui, S., Azzolin, L., Maimets, M., Maimets, M., Pedersen, M.T., Pedersen, M.T., Fordham, R.P., Hansen, S.L., Hansen, S.L., Larsen, H.L., Larsen, H.L., Guiu, J., Guiu, J., Alves, M.R.P., Alves, M.R.P., Rundsten, C.F., Rundsten, C.F., Johansen, J.V., Johansen, J.V., Li, Y., Li, Y., Madsen, C.D., Madsen, C.D., Nakamura, T., Watanabe, M., Nielsen, O.H., Schweiger, P.J., Piccolo, S., Jensen, K.B., 2018. YAP/TAZ-Dependent Reprogramming of Colonic Epithelium Links ECM Remodeling to Tissue Regeneration. Cell Stem Cell 22, 35–49.e7. doi:10.1016/j.stem.2017.11.001

Zhang, Y., Liu, T., Meyer, C.A., Eeckhoute, J., Johnson, D.S., Bernstein, B.E., Nusbaum, C., Myers, R.M., Brown, M., Li, W., Liu, X.S., 2008. Model-based analysis of ChIP-Seq (MACS). Genome Biol. 9, R137. doi:10.1186/gb-2008-9-9-r137